J. Fluid Mech. (1992), *vol.* 242, *pp.* 441–474
Printed in Great Britain

Linear and nonlinear stability of the Blasius boundary layer

By F. P. BERTOLOTTI[1], Th. HERBERT[2] AND P. R. SPALART[3]†

[1] ICASE NASA Langley Research Center, Hampton, VA 23665-5225, USA

[2] Department of Mechanical Engineeering, The Ohio State University, Columbus, OH 43210, USA

[3] NASA Ames Research Center, Moffet Field, CA 94035, USA

(Received 3 December 1990 and in revised form 17 February 1992)

Two new techniques for the study of the linear and nonlinear instability in growing boundary layers are presented. The first technique employs partial differential equations of parabolic type exploiting the slow change of the mean flow, disturbance velocity profiles, wavelengths, and growth rates in the streamwise direction. The second technique solves the Navier–Stokes equation for spatially evolving disturbances using buffer zones adjacent to the inflow and outflow boundaries. Results of both techniques are in excellent agreement. The linear and nonlinear development of Tollmien–Schlichting (TS) waves in the Blasius boundary layer is investigated with both techniques and with a local procedure based on a system of ordinary differential equations. The results are compared with previous work and the effects of non-parallelism and nonlinearly are clarified. The effect of nonparallelism is confirmed to be weak and, consequently, not responsible for the discrepancies between measurements and theoretical results for parallel flow. Experimental uncertainties, the adopted definition of the growth rate, and the transient initial evolution of the TS wave in vibrating-ribbon experiments probably cause the discrepancies. The effect of nonlinearity is consistent with previous weakly nonlinear theories. While nonlinear effects are small near branch I of the neutral curve, they are significant near branch II and delay or event prevent the decay of the wave.

1. Introduction

Currently, the preferred predictive method in industry for transition over complex aeronautical geometries rests on the Orr–Sommerfeld theory. To satisfy the basic assumption of a mean flow with parallel streamlines in this theory, the weak streamwise growth and the small transverse velocity of the flow are neglected. While much useful insight has been gained with this approach, there has long been interest in removing four of its deficiencies, namely (*a*) the neglect of mean flow non-parallelism; (*b*) whether the temporal growth rates are computed and then converted into spatial ones (Gaster 1962) or the spatial growth rates are solved for directly, the growth rate analysis incorrectly neglects the upstream history of the convected disturbances; (*c*) the nonlinear interaction between modes that leads the flow into turbulence is only roughly accounted for using an empirical correlation with experimental data usually the e^n-method (Smith & Gamberoni 1956; Van Ingen 1956); and (*d*) the receptivity dynamics through which free-stream and wall disturbance perturb the shear flow, are not modelled.

† Present address: Boeing Commercial Airplane Group, Seattle, WA 98124, USA.

As a contribution to the current body of models addressing the above deficiencies, we apply three methods for analysing the stability of boundary layers based on ordinary, parabolic partial, and elliptic partial differential equations, respectively. The latter two methods account for both non-parallel and nonlinear effects, as well as the upstream history of the disturbances. The method based on differential equations of parabolic type exploits the facts that the mean flow is governed by the boundary-layer approximation and, moreover, the second derivatives of the disturbance growth rate, wavelength, and velocity profile with respect to the streamwise diretion are sufficiently small to be neglected. While these facts have been used in previous multiple-scale analyses and the parabolic nature of the resulting intermediate equations has been mentioned by Gaster (1974), their potential for solving the stability problem has not been explored. These parabolic equations, which we denote as parabolized stability equations (PSE), describe the evolution of linear or nonlinear two- or three-dimensional disturbances in flows with combined slowly changing streamwise properties such as non-parallelism, real-gas effects, or dissociation, although we restrict the formulation here to the Blasius boundary layer. The PSE can be applied as well in parallel flows to study the temporal or spatial nonlinear evolution of initial data. The initial-boundary-value problem associated with the parabolic equations can be solved with a marching procedure. Initial conditions can be arbitrarily chosen or can be obtained from a local procedure. This procedure solves a homogeneous linear system of ordinary differential equations for local eigen-solutions similar to previous studies. Provided the derivation of this local procedure is mathematically justified (which it is only under limited circumstances), these eigensolutions agree with the solution of the linearized PSE within negligible differences. Given arbitrary initial conditions, the PSE solution will exhibit transient behaviour.

An alternative approach for studying the spatial evolution of disturbances in boundary layers including nonlinear and non-parallel effects is the direct numerical solution of the Navier–Stokes equations (DNS). Special attention must be paid to the non-physical outflow-boundary conditions to avoid the upstream reflection of energy of outflowing disturbances. Here we present a spectral method for solving the Navier–Stokes equations that avoids reflections using fringe regions adjacent to the inflow and outflow boundaries, yet maintains the benefits of using Fourier series in the streamwise and spanwise directions. The DNS approach takes no advantage of the essentially parabolic character of the disturbance evolution except in the fringe regions. Provided the fringe regions and streamwise periodic boundary conditions do not bias the solution, the DNS yield the benchmark for other approaches involving one or other approximation.

This paper consists of three major parts. Section 2 describes the parabolic stability equations and the associated eigenvalue problem for local solutions. Section 3 discusses the approach to solving the Navier–Stokes equations. Results of the various methods are presented in §4 for a comparison between each other and with previous work. Although the development of the PSE approach by Herbert & Bertolotti and of the DNS approach by Spalart occurred independently, we consider the side-by-side presentation of the two approaches and their results beneficial to both the verification of the new tools and the establishment of an accurate set of benchmark data for the non-parallel and nonlinear stability of the Blasius boundary layer.

1.1. *Previous work*

Numerous efforts have been made to avoid the approximations – parallel mean flow and linearization – in the stability analysis of boundary layers. The efforts regarding the mean flow have been motivated mainly by the fact that accurate numerical solutions of the Orr–Sommerfield equation show a discrepancy with experimental results on the neutral curve for two-dimensional Tollmien–Schlichting (TS) waves. Since these discrepancies are strongest at high frequency and low Reynolds number, the neglect of the boundary-layer growth has been considered the most likely cause.

The effect of non-parallelism in the Blasius boundary layer has been studied with the method of multiple scales by Bouthier (1972, 1973), Saric & Nayfeh (1977), Van Stijn & Van de Vooren (1983), and Bridges & Morris (1987), with an iterative method by Gaster (1974), and with an asymptotic expansion in the frequency by Itoh (1986). Bouthier concluded that, in contrast to the parallel case, the growth rate of disturbances in non-parallel flows depends on the distance from the plate and on the flow quantity considered and thus requires careful definition. Although this conclusion was confirmed in the subsequent studies, their results are different and puzzling. In terms of the preferred experimental measure $u'_{\max}$, the maximum streamwise r.m.s. fluctuation, Gaster found a neutral curve close to the parallel-flow result. While his findings were later confirmed by Van Stijn & Van de Vooren, Saric & Nayfeh presented a different neutral curve in better agreement with the experimental data. Moreover, their results were virtually confirmed by the measurements of Kachanov, Kozlov & Levchenko (1977). Bridges & Morris agreed with these results; meanwhile, the results of Saric & Nayfeh on the neutral curve were withdrawn. (Drazin & Reed 1981, Addendum.)

The most direct attempt to obtain stability results for two-dimensional disturbances has been made by Fasel (1976) by solving the Navier–Stokes equations numerically. The key to this success was the formulation of non-reflective artificial outflow-boundary conditions, a problem that is still unsolved for more general disturbances. In a similar approach, Bayliss *et al.* (1985) obtained results for the streamwise evolution of linear and nonlinear TS waves. These numerical studies, however, did not resolve the discrepancies between experiment and theory. Recently, Fasel & Konzelmann (1990) investigated the non-parallel effects on small-amplitude disturbances in the Blasius boundary layer using a direct Navier–Stokes solver and clarified some of the main differences in past results.

A theoretical model capturing the combined effects of non-parallelism and nonlinearity has long been desired. The attempt to incorporate nonlinear effects in the multiple-scales approach fails, however, since the crucial solvability condition determines only one correction, either for non-parallelism or nonlinearity. This weakness of the non-parallel stability theory is probably caused by accounting for small terms of the same order at different levels of approximation, a procedure that is not rational in the sense of Van Dyke (1975).

Using the parallel flow approximation, Itoh (1974) and Herbert (1974) applied perturbation methods to incorporate the effect of nonlinearity on the growth of two-dimensional waves and partially overcame the problem in representing the mean-flow distortion. In a strictly parallel framework, no mean-flow solution to the Navier–Stokes or boundary-layer equations exists in a semi-infinite domain. The results demonstrated a stabilizing effect of nonlinearity near the critical point and the lower branch of the neutral curve, while this effect is destabilizing near the upper

branch at higher Reynolds numbers. In the absence of systematic experiments, the results could not be substantiated.

More recently, asymptotic theories valid in the limit of infinite Reynolds number incorporated the effects of non-parallelism and nonlinearity simultaneously (Smith 1979*a*, *b*; Goldstein & Durbin 1986). Smith found the lower branch of the neutral curve similar to Saric & Nayfeh (1977) and concluded that accounting for non-parallelism improved the agreement with the experimental data. However, the accuracy of the asymptotic results at the relatively low Reynolds numbers of concern was not verified.

Smith, Papgeorgiou & Elliot (1984), studied the stability of plane Poiseuille and Blasius flow by numerically solving an extended form of the interactive boundary-layer equations that can capture both the triple-decked and the quintuple-decked structures at the lower and upper branches, respectively, of the neutral curve. These equations are obtained from the Navier–Stokes equation by neglecting streamwise diffusion terms and the convective acceleration term involving the product of the plate normal velocity. Outside the boundary-layer the equations match with the usual outer deck. The outer deck is elliptic, but the authors noted that limiting the domain to within the boundary layer 'turns out to work numerically', in agreement with the parabolic character of our formulation. The streamwise parabolic character of the equations, however, was neglected when use was made of the temporal growth model, along with the parallel-flow approximation and streamwise-periodic flow. In the linearized case, the equations were combined into one that is contained within the Orr–Sommerfield equation, and the corresponding spectra were found to be similar. In the nonlinear case the Fourier expansion in wavenumber lead to coupled equations that were numerically solved using a finite-difference formulation in time. Comparison of results to those given by the Navier–Stokes equations showed that the difference remained small, suggesting that the neglected terms are not part of 'the dominant terms and balances in the unsteady Navier–Stokes equations'.

The use of parabolic differential equations in the analysis of problems of basically elliptic nature with small feedback is successful in some other areas, e.g. in the analysis of acoustic wave propagation (McAninch 1986). In the field of weakly non-parallel flow stability, Hall (1983) suggested solving parabolic equations for steady Görtler vortices describing the evolution within terms of order $O(R_x^{-1})$, where R_x is the Reynolds number based on the streamwise variable. In essence, this approach considers Görtler vortices a three-dimensional solution of the boundary-layer equations. For steady, spanwise-periodic disturbances, Hall's equations are a special case of the PSE formulated in curvilinear coordinates. Itoh (1986) derived a parabolic equation for small-amplitudes TS waves identical with the linearized PSE for two-dimensional disturbances. Itoh observed that his equation contains both the unsteady boundary-layer equation and the Orr–Sommerfeld equation as limits, hence its solutions can directly describe the matching of solutions shown with asymptotic methods by Goldstein (1983). Since separation of variables is inapplicable, Itoh choose an asymptotic expansion in frequency to reduce the problem to a sequence of ordinary differential equations.

2. The parabolic stability equations

The development leading to the parabolic stability equations is applicable to a wide range of convectively unstable flows. For brevity and without loss of generality we consider two-dimensional disturbances in the Blasius boundary layer. The

extension to three-dimensional disturbances can be found in Herbert (1991) and in a more extended description in Bertolotti (1991).

We use Cartesian coordinates x, y, where x is the streamwise direction and y is normal to the plate. The Navier–Stokes equations are written in terms of the stream function Ψ to satisfy continuity identically,

$$\left(\frac{\partial}{\partial t}-\frac{1}{R_0}\nabla^2+\frac{\partial \Psi}{\partial y}\frac{\partial}{\partial x}-\frac{\partial \Psi}{\partial x}\frac{\partial}{\partial \Psi}\right)\nabla^2\Psi=0. \tag{1}$$

All quantities are non-dimensionalized using the velocity U_∞ and the fixed length $\delta_0=\delta(x_0)=(\nu\tilde{x}_0/U_\infty)^{\frac{1}{2}}$, where $\tilde{x}_0$ is a dimensional distance from the leading edge, here taken to be the starting location of the analysis, and ν is the kinematic viscosity. $R_0=U_\infty\delta_0/\nu$ is the Reynolds number based on δ_0. We further note the relations $x_0=\tilde{x}_0/\delta_0=R_0$, and $R=(x/x_0)^{\frac{1}{2}}R_0=(\nu\tilde{x}/U_\infty)^{\frac{1}{2}}$, where R is the Reynolds number based on $\delta(x)$.

We decompose the stream function into the disturbance $\psi(x,y,t)$ and the mean flow $\Psi_{\mathrm{B}}(x,y)$ that is given within the boundary-layer approximation by $\Psi_{\mathrm{B}}=f(\eta)(x/x_0)^{\frac{1}{2}}+O(R^{-2})$, where f satisfies the Blasius equation

$$\begin{gathered} f'''+\tfrac{1}{2}ff''=0, \\ f=f'=0 \quad \text{at} \quad \eta=0, \quad f'\to 1 \quad \text{as} \quad \eta\to\infty, \end{gathered} \tag{2}$$

with $\eta=\tilde{y}/\delta(\tilde{x})$, and $\tilde{y}$ is the dimensional coordinate normal to the plate. The nonlinear equation governing the disturbance ψ is obtained by introducing the combined flow into the Navier–Stokes equation and subtracting the equation satisfied by the mean flow:

$$\begin{aligned} &\left(\frac{\partial}{\partial t}-\frac{1}{R_0}\nabla^2+\frac{\partial \Psi_{\mathrm{B}}}{\partial y}\frac{\partial}{\partial x}-\frac{\partial \Psi_{\mathrm{B}}}{\partial x}\frac{\partial}{\partial y}\right)\nabla^2\psi \\ &\qquad+\frac{\partial \psi}{\partial y}\frac{\partial^3\Psi_{\mathrm{B}}}{\partial x\,\partial y^2}-\frac{\partial \psi}{\partial x}\frac{\partial^3\Psi_{\mathrm{B}}}{\partial y^3}=\left(\frac{\partial \psi}{\partial x}\frac{\partial}{\partial y}-\frac{\partial \psi}{\partial y}\frac{\partial}{\partial x}\right)\nabla^2\psi+O(R^{-2}), \end{aligned} \tag{3}$$

where the errors of order $O(R^{-2})$ are introduced by the boundary-layer approximation to the mean flow.

This equation supports solutions in the form of waves. Applying the boundary-layer approximation directly to this equation to obtain one similar to the unsteady parabolized Navier–Stokes equation would be incorrect since the relatively short wavelength of instability waves causes streamwise changes too large to be neglected (Herbert & Morkovin 1980). However, parabolic equations for the slowly varying components of the solution can be obtained by accounting separately for the wave-like nature on the disturbance, as will next be shown for a single-frequency wave governed by the linearized version of (3). Inclusion of the nonlinear terms produces a coupled set of parabolic equations, as will be discussed later.

A spatially evolving two-dimensional wave of constant frequency ω is described by specifying the streamwise wavenumber $\alpha(x)$, the exponential growth rate $\gamma(x)$, and the velocity profiles as derivatives of the complex stream function $\phi(x,y)$. These quantities are combined to represent the disturbance stream function in the form

$$\psi(x,y,t)=\phi(x,y)\,\chi(x,t)+\text{c.c.}, \tag{4}$$

where

$$\chi(x,t)=\exp\left[\int_{x_0}^{x}a(\zeta)\,\mathrm{d}\zeta-\mathrm{i}\omega t\right],$$

$$a(x)=\gamma(x)+\mathrm{i}\alpha(x),$$

and c.c. stands for the complex conjugate.

The partition of ψ into χ and ϕ in (4) resembles the normal mode form used in the Orr–Sommerfeld theory, where χ models the wave-like nature of the disturbance and ϕ models the slowly changing profile. Previous investigators further reduced the problem to ordinary differential equations by employing an expansion in a slow streamwise variable in the form

$$\phi(x, y) = \phi_0(\epsilon x, y) + \epsilon\phi_1(\epsilon x, y),$$
$$a(x) = a_0(\epsilon x) + \epsilon a_1(\epsilon x),$$

where ϵ is a small parameter of order $O(R^{-1})$. The solution is obtained by solving the governing ordinary differential equations for ϕ_0, a_0 and ϕ_1, a_1 in succession. Such an expansion is used, for example, in the method of multiple scales. However, this approach introduces two fundamental shortcomings which are absent in the formulations of the PSE. First, application of the expansion to nonlinear problems gives rise to two unrelated expansion parameters measuring the non-parallelism and the amplitude, respectively, and consequently requires arranging the governing equations in hierarchical order. This shortcoming is not present in the PSE analysis because all terms are treated simultaneously. The second problem occurs when the wavelength of the disturbance becomes sufficiently long to reduce the order of the convective acceleration terms to that of the viscous forces, namely $O(R^{-1})$. Except in the unlikely case of a self-similar disturbance flow field (i.e. neither growing or decaying), the flow field cannot be approximated by solutions to a succession of ordinary differential equations. The nonlinear PSE, on the other hand, correctly approaches the unsteady boundary-layer equation in this limit. Steady two-dimensional disturbances with an infinite streamwise wavelength occur in the form of the mean-flow distortion that is generated by nonlinear mode interaction, and in three-dimensional flows in the form of streamwise vortices generated by surface curvature, crossflow instability, and by nonlinear mode interaction.

For fixed free-stream velocity and viscosity, hence fixed R_0, the dependence of a and ϕ on x results from the non-parallelism of the mean flow that renders (3) non-separable in x and y. In general, the dependence on x can result from non-parallelism and nonlinearity. Since both ϕ and χ depend on x, the partition of ψ into ϕ and χ in (4) is ambiguous. Indeed, a part of the exponential factor an be included in ϕ without any change in the form of the partition. The partition becomes beneficial when the analysis is applied to flows in which disturbances exhibit the following two properties:

(P1) The velocity profiles, wavelengths, and growth rates change slowly in the streamwise direction. Hence, in the formulation of (4), there exist values of γ and α such that $\partial^2 a/\partial x^2$ and $\partial^2\phi/\partial x^2$ and products of first derivatives $\partial a/\partial x$, $\partial\phi/\partial x$ are negligibly small.

(P2) The disturbances grow and decay as convected instabilities. No self-sustained oscillation in any region of the mean flow is possible. The mean flow acts purely as an amplifier of incoming free-stream disturbances and, in their absence, the flow returns to its undisturbed state (Huerre & Monkewitz 1990).

Under the conditions (P1) and (P2), a normalization condition can be specified such that ϕ and a become slowly varying functions of x. Then the analysis leads naturally to parabolic equations governing the evolution of ϕ and a since the second derivatives of these quantities with respect to x are negligible.

The assumption that these properties hold is inherent in all the aforementioned

analyses. Property (P2) implies that the instabilities exhibit a negligible dependence on downstream conditions and produce an equally negligible upstream influence. Direct Navier–Stokes solvers with an outflow boundary condition make use of this property (within the boundary layer).

Property (P1) has been observed to hold for TS waves both in experiments and in numerical computations. A supporting argument can be derived from Morkovin's (1985) observation that the maximum amplification of small-amplitude TS waves occurs when a positive feedback loop exists between the two viscosity-dominated regions, the critical layer and the Stokes layer at the wall, and that the ratio of Stokes layer thickness to the distance of the critical layer from the wall remains practically constant along the ridge of maximum TS wave amplification in the frequency–Reynolds-number plane for $1.22\times10^5 < R_x < 8.44\times10^8$. Since the location the critical layer depends on the u velocity profile of the mean flow, we can conclude that the growth of the boundary layer tunes and detunes the feedback loop and it is plausible to expect changes in γ and α with x to occur on a similar scale as the divergence of the mean flow.

This argument does not carry into the nonlinear region, but simulations of the three-dimensional breakdown of TS waves by using the PSE (Herbert & Bertolotti 1991) show that (P1) and (P2) hold up to the spike stage. Further supporting evidence can be inferred from the agreement between temporal and spatial DNS simulations since in the former case the streamwise boundary conditions are periodic and the complex velocity profiles vary only with y and t.

With property (P1), the derivatives of ψ with respect to x are linear in $\partial\phi/\partial x$ and $\mathrm{d}a/\mathrm{d}x$, and take the simple form

$$\frac{\partial^m\psi}{\partial x^m} = \left[a^m\phi + ma^{m-1}\frac{\partial\phi}{\partial x} + \frac{m}{2}(m-1)\,a^{m-2}\frac{\mathrm{d}a}{\mathrm{d}x}\phi\right]\chi + \text{c.c.} \tag{5}$$

Introducing this result in the disturbance equation (3) yields a partial differential equation of parabolic type that is the first of two equations which comprise the PSE. The parabolic character is clearly exhibited when the linearized equation for two-dimensional disturbances is written in operator form,

$$(\mathrm{L}_0+\mathrm{L}_1)\,\phi + \mathrm{L}_2\frac{\partial\phi}{\partial x} + \frac{\mathrm{d}a}{\mathrm{d}x}\mathrm{L}_3\,\phi = 0, \tag{6a}$$

with boundary conditions

$$\phi(x,0) = \frac{\partial}{\partial y}\phi(x,0) = 0, \quad \phi(x,y) = \frac{\partial}{\partial y}\phi(x,y) = 0 \quad \text{as} \quad y\to\infty, \tag{6b}$$

and initial conditions

$$\phi(x_0,y) = f(y), \quad a(x_0) = a_0. \tag{6c}$$

The operators L_0 to L_3 operate only in y and are

$$\mathrm{L}_0 = -\frac{1}{R}(\mathrm{D}^2+a^2)^2 + \left(\frac{\partial\Psi_{\mathrm{B}}}{\partial y}a - \mathrm{i}\omega\right)(\mathrm{D}^2+a^2) - \frac{\partial^3\Psi_{\mathrm{B}}}{\partial y^3}a, \tag{7a}$$

$$\mathrm{L}_1 = \frac{\partial^3\Psi_{\mathrm{B}}}{\partial x\,\partial y^2}\mathrm{D} - \frac{\partial\Psi_{\mathrm{B}}}{\partial x}(\mathrm{D}^2+a^2)\,\mathrm{D}, \tag{7b}$$

$$\mathrm{L}_2 = -\frac{4a}{R}(\mathrm{D}^2+a^2) + \frac{\partial\Psi_{\mathrm{B}}}{\partial y}(\mathrm{D}^2+3a^2) - 2\mathrm{i}\omega a - \frac{\partial^3\Psi_{\mathrm{B}}}{\partial y^3}, \tag{7c}$$

$$L_3 = -\frac{2}{R}(D^2+3a^2) - i\omega + \frac{\partial \Psi_B}{\partial y} 3a, \tag{7d}$$

with $D = \partial/\partial y$. L_0 is the Orr–Sommerfeld operator and L_1 accounts for the transverse velocity component of the mean flow.

A second equation is required to resolve the ambiguity in partitioning ψ in (4) into two functions of x. Clearly, we wish to exploit this ambiguity such that the computed values of a and ϕ satisfy (P1). We achieve this by specifying a normalization on ϕ which restricts rapid changes in x. Possible choices are

$$\frac{\partial \phi(x, y_m)}{\partial x} = 0, \quad \frac{\partial \hat{u}(x, y_m)}{\partial x} = 0, \quad \int_0^\infty \frac{\partial \hat{u}}{\partial x} \hat{u}^\dagger \, dy = 0, \tag{8a–c}$$

for all $x \geqslant x_0$. Here, $\hat{u} = \partial\phi/\partial y$ is the complex velocity profile, $\dagger$ denotes the complex conjugate, and y_m is some chosen location, usually the point where $|\hat{u}|$ reaches a maximum. The normalization condition specifies how much growth and sinusoidal variation is represented by the exponential function χ and the profile ϕ, respectively. This partition varies slightly with the normalization employed; however, the growth rate based on physical quantities will be independent of the of the choice of normalization, as discussed below. Equations (6) and (8) comprise the linearized parabolic stability equations that govern the evolution of the unknown functions a and ϕ.

In special limits, the linearized PSE equation (6a) is equivalent to equations used in previous studies. At high Reynolds numbers, when the non-parallel effects are very small, (6a) approaches the Orr–Sommerfeld equation. At low Reynolds numbers and low frequencies, the wavenumber becomes small and powers of a become negligible. In this limit, (6a) approaches the unforced unsteady boundary-layer equation used in receptivity analyses. Itoh (1986) exploited this property to verify the matched asymptotic expansions of Goldstein (1983). If streamwise curvature is included, the PSE for three-dimensional disturbances contain the parabolic differential equations for Görtler vortices given by Hall (1983).

2.1. *The nonlinear problem*

The evolution of a TS wave, with frequency ω and wavenumber α, from infinitesmal to finite amplitude is accompanied by the rise of the harmonics having frequencies $n\omega$, $n = 2, 3, \ldots$, as well as a steady mean-flow distortion ($n = 0$). The phase speed of the harmonics will be equal, or nearly equal, to that of the TS wave, since otherwise the finite-amplitude structure would disperse. Thus, we set the wavenumber of the harmonics equal to $n\alpha$, and represent the flow field as

$$\psi(x, y, t) = \Psi_B(x, y) + \sum_{n=-\infty}^{\infty} \phi_n(x, y) \exp\left[\int_{x_0}^{x} a_n(\zeta)\, d\zeta - in\omega t\right], \tag{9}$$

where $a_n = \gamma_n + in\alpha$. Property (P1) is assumed to extend to all harmonics. Inserting the expansion (9) into the disturbance equation (3), using (5), and performing harmonic balance in the frequency yields a set of coupled nonlinear equations of the form:

$$\left[(L_0(a_n) + L_1(a_n))\,\phi_n + L_2(a_n)\frac{\partial \phi_n}{\partial x}\right] \exp\left[\int_{x_0}^{x} a_n(\zeta)\, d\zeta\right]$$
$$= \sum_{m=-\infty}^{\infty} N[a_m, a_{n-m}, \phi_m(x, y), \phi_{n-m}(x, y)] \exp\left[\int_{x_0}^{x} (a_m + a_{n-m})\, d\zeta\right], \tag{10a}$$

where

$$\mathrm{N}(a,b,\phi_a,\phi_b) = \left(a\phi_a + \frac{\partial\phi_a}{\partial x}\right)\left(b^2\frac{\partial\phi_b}{\partial y} + 2b\frac{\partial^2\phi_b}{\partial x\,\partial y} + \frac{\partial^3\phi_b}{\partial y^3}\right) - \frac{\partial\phi_a}{\partial y}\left(b^3\phi_b + 3b^2\frac{\partial\phi_b}{\partial x} + b\frac{\partial^2\phi_b}{\partial y^2} + \frac{\partial^3\phi_b}{\partial x\,\partial y^2}\right).$$

The operators L_0, L_1, L_2 and N depend nonlinearly on $a_n(x)$. Comparison of the left-hand sides of (10*a*) and (6*a*) shows that we have specified $\mathrm{d}a_n/\mathrm{d}x = 0$. We use this approximation to simplify (10*a*) but note that its use is not a necessary step in the formulation. This topic is further discussed in §2.3. The boundary conditions are

$$\phi_n = \frac{\partial\phi_n}{\partial y} = 0 \quad \text{at} \quad y = 0, \quad y\to\infty, \quad n = 1,2,3,\ldots, \tag{10b}$$

$$\phi_0 = \frac{\partial\phi_0}{\partial y} = \frac{\partial^3\phi_0}{\partial y^3} = 0 \quad \text{at} \quad y = 0, \quad \frac{\partial\phi_0}{\partial y} = 0 \quad \text{as} \quad y\to\infty. \tag{10c}$$

The boundary conditions for the oscillatory Fourier components $n > 0$ require vanishing u and v velocities at the wall and at infinity. The boundary conditions for the mean flow distortion replace the condition $v = 0$ at infinity to allow a variation of the displacement thickness, as required by the boundary-layer approximation. To complete the formulation of the PSE, a normalization condition is imposed on every mode. At finite amplitudes, the velocity profiles of the TS wave and the harmonics may develop multiple local maxima, and it is more appropriate to specify a normalization of the integral of $\hat{u}$ as in (8*c*) rather than on $u'_{\max}$ as in (8*b*),

$$\mathrm{Re}\left[\int_0^\infty \frac{\partial\hat{u}_n}{\partial x}\hat{u}_n^\dagger\,\mathrm{d}y\right] = 0, \quad n = 0,1,2,\ldots,n, \tag{11a}$$

$$\mathrm{Im}\left[\int_0^\infty \frac{\partial\hat{u}_1}{\partial x}\hat{u}_1^\dagger\,\mathrm{d}y\right] = 0. \tag{11b}$$

Equations (10) and (11) provide $2n+3$ equations for the $2n+3$ unknowns,

$$\phi_n(x,y), \quad \gamma_n(x), \quad \alpha(x), \quad n = 0,1,2,\ldots,n. \tag{12}$$

We note that, in contrast to weakly nonlinear theories, the PSE formulation does not require a hierarchical ordering of terms based on amplitude. The convergence of series (9) is maintained during the marching procedure by introducing new harmonics, (i.e. increasing the cutoff N), when these harmonics are forced by a right-hand side that is greater than a pre-set threshold. This threshold is selected at less than order $O(R^{-2})$, consistent with the order of the neglected streamwise derivatives.

2.2. *Measures of growth*

In the parallel-flow approximation, all physical quantities grow or decay according to the eigenvalue of the Orr–Sommerfeld equation in exactly the same way. In a non-parallel mean flow, the growth and phase variation of some physical quantity Q depends on a, ϕ, and possibly the y-derivatives of ϕ. The growth rate of Q is defined as the logarithmic derivative

$$\bar{\gamma}(x) = \frac{1}{Q}\frac{\partial Q}{\partial x}, \tag{13}$$

where the division by Q renders the result independent of the magnitude of Q.

Growth rates have been predominantly based on velocities. We denote the real physical velocities by u, v, the root-mean-square velocities by u', v', and the complex velocity profiles in the mathematical formulation by $\hat{u}$, $\hat{v}$.

As observed by Bouthier (1973), the dependence of ϕ on y makes the growth rate at each streamwise location ambiguous since different rates are obtained at different distance from the wall. Furthermore, as discussed by Schubauer & Skramstad (1947), Gaster (1965), and Saric & Nayfeh (1977), the growth rate is affected by the direction, say $Y = Y(x)$, along which the streamwise derivative of Q is taken. Van Stijn & Van de Vooren (1983) further noted that the growth rate based on the maximum of u' at y_m is independent of the direction $Y(x)$.

The streamwise change of u'_{max} is indeed a good measure for the growth of small-amplitude disturbance for various reasons. The experimental measurements of the u-component are more accurate than those of the v-component. Growth data based on u'_{max} are independent of the path traversed by the sensor and avoid the need to determine the exact height of the sensor above the plate. In addition, the amplitude based on u'_{max} is proportional to the strength of the vorticity at the critical layer that plays a central role in the evolution of secondary instabilities. The growth rate and wavenumber based on u'_{max} are given by

$$\bar{\gamma}(x) = \gamma(x) + \mathrm{Re}\left[\frac{1}{\hat{u}(x, y_m)} \frac{\partial \hat{u}(x, y_m)}{\partial x}\right], \tag{14a}$$

$$\bar{\alpha}(x) = \alpha(x) + \mathrm{Im}\left[\frac{1}{\hat{u}(x, y_m)} \frac{\partial \hat{u}(x, y_m)}{\partial x}\right]. \tag{14b}$$

Other quantities such as the disturbance energy can be monitored for growth. With some exceptions, e.g. the growth of u at the point where u changes phase, growth rates and wavenumbers based on different quantities agree within $O(R^{-1})$. However, neutral stability curves can differ widely at the higher frequencies where the growth rate is of the same order.

2.3. *On the normalization condition*

We expand the discussion on the normalization condition, (8), that supplies the equation needed for the evaluation $a(x) = \gamma(x) + i\alpha(x)$. The left-hand-side of (8c) is an inner product, $\langle \hat{u}, \hat{u}_x \rangle$. This inner product lets us define the projection of $\hat{u}_x$ onto $\hat{u}$, denoted b, and computed as

$$b = \langle \hat{u}, \hat{u}_x \rangle / \langle \hat{u}, \hat{u} \rangle. \tag{15}$$

The function

$$r(x, y) = \hat{u}_x - b\hat{u}$$

is the component of $\hat{u}_x$ orthogonal to $\hat{u}$. Clearly, when $r = 0$ then $\hat{u} \sim e^{bx}$, so that $b + a$ yields, locally, the total exponential change of $u = \hat{u}\chi$. The orthogonal decomposition $\hat{u}_x = b\hat{u} + r$ helps us understand the normalization condition, as follows.

Given the values of a_j and $\hat{u}_j$ at x_j, we take a step forward to x_{j+1} keeping $a = a_j$ and solving (6a) for $\hat{u}_{j+1}$. Using the finite-difference representation for $\hat{u}_x$ in (15), we obtain

$$b_{j+1} = \langle \hat{u}_j, (\hat{u}_{j+1} - \hat{u}_j)/\Delta x \rangle / \langle \hat{u}_j, \hat{u}_j \rangle, \tag{16}$$

with the corresponding decomposition

$$\hat{u}_{j+1} = (1 + b_{j+1}\Delta x)\, \hat{u}_{j+1}. \tag{17}$$

The rapid growth of $|\hat{u}_j|$ with j can be most easily seen in the case of constant b. In practice b_j may vary, but the variation does not alter the results of this analysis in a significant way. For constant b the solution to (17) is

$$\hat{u}_j = \hat{u}_0 (1 + b\Delta x)^j + f_j,$$

where f is the particular solution, whose exact form does not concern us here. What is of concern is the exponential growth of $\hat{u}_j$ for non-zero b; this growth may violate the assumption of a slowing changing profile with x. It is necessary, thus, to keep $|b_j| \ll 1$ at every step. The magnitude of $|b_{j+1}|$ in (16) depends on the value of a used during the marching step. If $|b_{j+1}|$ is non zero, we can repeat the marching step with an updated value of the exponent a to obtain a new smaller value of $|b_{j+1}|$. In particular, if we repeat the step from x_j to x_{j+1} using $a = a_j + b_{j+1}^{(1)}$, where the superscript (1) on b_{j+1} denotes the value obtained in our first iterate of the marching step, and compute $b_{j+1}^{(2)}$, we obtain $|b_{j+1}^{(2)}| < |b_{j+1}^{(1)}|$. We can repeat the step again using $a = a_j + b_{j+1}^{(1)} + b_{j+1}^{(2)}$, to obtain $|b_{j+1}^{(3)}| < |b_{j+1}^{(2)}| < |b_{j+1}^{(1)}|$, and so on until $|b_{j+1}^{(n)}|$ is as small as desired. Indeed, there exists a value $a = a_{j+1}$ for which $b_{j+1} = 0$, that is, for which (8c) is satisfied.

Thus, condition (8c) provides the unique value of $a(x)$ that removes from $\hat{u}_x$ any exponential change (i.e. both growth and rotation) measured by b in (15). The profile $\hat{u}$, then, contains only the remainder r that captures the slow, $O(R^{-1})$, streamwise variation of the profile. The above discussion is equally applicable when one chooses (8b) as the normalization condition, since (8b) can be seen as a special case of (8c) with a Dirac delta function multiplying the integrand.

Our numerical investigations show that the values of $a(x)$ obtained using (8b) and (8c) differ slightly. This arbitrariness is of no concern, however, since it only affects the partition (4). The corresponding growth rates based on a physical quantity, as presented in §2.2, are equal to within the order of our approximation, $O(R^{-2})$.

Lastly, we observe that since the growth from x_j to x_{j+1}, holding a constant, is of magnitude $|1 + b\Delta x|$, a restriction exists on the step size Δx. If the step is too large and b is non-zero, the growth of $\hat{u}_{j+1}$ may violate the assumption of slow variation with x. As shown below, however, this restriction is not too severe, so that the limiting step size is far larger than the step size needed to resolve branch I and branch II with acceptable accuracy.

2.4. *Numerical formulation*

The semi-infinite domain, $y \in [0, \infty)$, is mapped algebraically to $\bar{y} \in [1, 0)$ using

$$\bar{y} = \frac{y_0}{y_0 + y}, \tag{18}$$

where y_0 is a suitably chosen parameter. The function $\phi(x, y)$ and operators L_i are approximated by vector $\boldsymbol{\phi}(x)$ and matrices $\boldsymbol{M}_i(x)$, respectively, using a spectral collocation method in $\hat{y}$. The parameter y_0 controls the distribution of collocation points in the physical domain. If not otherwise stated, the results presented here have been obtained using 40 Chebyshev polynomials. The profiles for modes $n > 0$ are expanded in a series of odd polynomials that automatically satisfy the far-field boundary condition, while even polynomials are used for the mean-flow distortion mode.

The streamwise derivative, $\partial\boldsymbol{\phi}(x)/\partial x$ is approximated by the finite-difference form $(\boldsymbol{\phi}_{j+1} - \boldsymbol{\phi}_j)/\Delta x_j$, where j is the step index. Owing to the appearance of a in the operators L_i, the system (6) is nonlinear. Iteration is employed to solve the nonlinear algebraic system exactly at the midpoint of the interval, where the finite difference form of $\partial/\partial x$ is second-order accurate. The iteration employs a predictor–corrector approach that corrects the value of a until the normalization condition (8b) is satisfied. The convergence of the iteration is monitored during every step, and the marching procedure terminates if the equation fails to be satisfied within a given error limit.

The collocation and trapezoidal procedures lead to an algebraic system of the form:

$$(\boldsymbol{M}_0+\boldsymbol{M}_1)[\boldsymbol{\phi}_{j+1/2}]+\boldsymbol{M}_2[\boldsymbol{\phi}_{j+1}-\boldsymbol{\phi}_j]/\Delta x=0, \tag{19}$$

where the matrices $\boldsymbol{M}_i$ are evaluated with the values of Ψ_{B} and a at the midpoint of the step, and

$$\boldsymbol{\phi}_{j+1/2}=\tfrac{1}{2}(\boldsymbol{\phi}_{j+1}+\boldsymbol{\phi}_j).$$

The iteration is composed of two parts, the first of which solves (19) for $\boldsymbol{\phi}_{j+1}$, followed by the modification of the growth rate γ and the wavenumber α according to the finite difference form of the normalization (8*b*),

$$\Delta\gamma_{j+1}=\frac{2}{\Delta x}\,\mathrm{Re}\left[\frac{(\hat{u}_{j+1})_{\max}-(\hat{u}_j)_{\max}}{(\hat{u}_{j+1})_{\max}+(\hat{u}_j)_{\max}}\right], \tag{20a}$$

$$\Delta\alpha_{j+1}=\frac{2}{\Delta x}\,\mathrm{Im}\left[\frac{(\hat{u}_{j+1})_{\max}-(\hat{u}_j)_{\max}}{(\hat{u}_{j+1})_{\max}+(\hat{u}_j)_{\max}}\right], \tag{20b}$$

where the subscript max indicates evaluation at y_{m}, the location where $|\hat{u}_j|$ attains its maximum. During the iteration procedure, (20*a*) and (20*b*) transfer the growth and the rotation in the complex plane, respectively, of $\hat{u}_{\max}$ into the function χ. The iteration is continued until the largest modification is less than 10^{-8}. The process is repeated at the next marching step.

We found it beneficial to use an implicit Euler formula during the initial steps to increase the damping of transients created by the initial conditions. We change the finite-difference formula gradually to the Crank–Nicolson formula as the integration progresses downstream to improve the convergence of the iterative process.

The extension to the nonlinear problem is accomplished by applying the above procedure to each mode $\boldsymbol{\phi}_n$, leading to a coupled nonlinear algebraic system of the form

$$\begin{aligned}(\boldsymbol{M}_0+\boldsymbol{M}_1)[\boldsymbol{\phi}_{n,j+1/2}]+\boldsymbol{M}_2[\boldsymbol{\phi}_{n,j+1}-\boldsymbol{\phi}_{n,j}]/\Delta x\\ =\sum_{m=-\infty}^{\infty}N(\boldsymbol{\phi}_{m,j+1/2},\boldsymbol{\phi}_{n-m,j+1/2})A_{m,j+1/2}A_{n-m,j+1/2}/A_{n,j+1/2}\end{aligned} \tag{21}$$

for the unknowns (12). The amplitudes are evaluated at the midpoint of the step,

$$A_{n,j+1/2}=A_n(x_0)\exp\left[\int_{x_0}^{x_{j+1/2}}\gamma_n(\zeta)\,\mathrm{d}\zeta\right].$$

The first part of the iteration solves $\boldsymbol{\phi}_{n,j+1}$ for each n. In the second part, the normalization (8*c*) is applied to obtain the modification of the growth rates γ_n,

$$\Delta\gamma_{n,j+1}=\mathrm{Re}\left[\left(\sum_0^{\infty}\hat{u}_{n,j+1}\hat{u}^{\dagger}_{nj+1}\,dy\right)^{-1}\int_0^{\infty}\frac{\partial\hat{u}_{n,j+1}}{\partial x}\hat{u}^{\dagger}_{n,j+1}\,\mathrm{d}y\right], \tag{22a}$$

and the modification to the wavenumber α of the TS wave,

$$\Delta\alpha_{j+1}=\mathrm{Im}\left[\left(\int_0^{\infty}\hat{u}_{1,j+1}\hat{u}^{\dagger}_{1,j+1}\,\mathrm{d}y\right)^{-1}\int_0^{\infty}\frac{\partial\hat{u}_{1,j+1}}{\partial x}\hat{u}^{\dagger}_{1,j+1}\,\mathrm{d}y\right], \tag{22b}$$

transferring the average growth of the complex quantities $\int_0^{\infty}(\partial\hat{u}_n/\partial x)\,\mathrm{d}y$ into χ_n. The iteration is continued until the largest modification is less than 10^{-8}, after which the process is repeated for the next step in x.

2.5. *Local solutions*

To obtain pointwise results on stability and to generate the initial conditions (6*b*) for stability analysis with the PSE, we apply a local procedure that uses only the mean-flow and the disturbance parameters at some streamwise location x_0, say. If the amplitude of the TS wave is sufficiently small for linearization, this local procedure is similar to that introduced by Bouthier (1972) and later applied by others, yet our derivation appears much simpler and provides a more consistent formal approach. In particular, this approach permits accounting for both non-parallelism and non-linearity. Therefore, the finite-amplitude TS waves, the local procedure can be coupled with a Landau expansion in the amplitude (Bertolotti 1991). In any case, the local procedure rests on ordinary differential equations that govern the properties of the solution in the neighbourhood of x_0. Here, we present only the linear procedure to obtain the unknown quantities ϕ, $\partial\phi/\partial x$, a, and $\mathrm{d}a/\mathrm{d}x$ in (6) for given parameters ω, R_0, and the mean-flow $\boldsymbol{\Psi}_{\mathrm{B}}$.

We introduce a Taylor expansion for ϕ, a and the mean-flow $\boldsymbol{\Psi}_{\mathrm{B}}$ with respect to the variable $\xi = x - x_0$ and note that higher derivatives can be neglected within property (P1) and the boundary-layer approximation to the mean flow. We obtain

$$\phi(x,y) = \phi_0 + \xi\phi_1, \quad a(x) = a_0 + \xi a_1,$$

and a similar expansion for the mean flow, where

$$\phi_0(y) = \phi(x_0,y), \quad \phi_1(y) = \left.\frac{\partial\phi(x,y)}{\partial x}\right|_{x_0}, \quad a_0 = a(x_0), \quad a_1 = \left.\frac{\mathrm{d}a(x)}{\mathrm{d}x}\right|_{x_0}.$$

The disturbance stream function takes the form

$$\psi(x,y,t) = (\phi_0 + \xi\phi_1)\exp\left[\int_0^{\xi}(a_0 + a_1)\,\mathrm{d}\zeta - \mathrm{i}\omega t\right]. \tag{23}$$

Introducing this expression into (6) and requiring the equation to be valid for varying ξ provides two equations,

$$(\mathrm{L}_0 + \mathrm{L}_1 + a_1\,\mathrm{L}_3)\,\phi_0 + \mathrm{L}_2\,\phi_1 = 0, \tag{24a}$$

$$(\mathrm{L}_4 + a_1\,\mathrm{L}_2)\,\phi_0 + \mathrm{L}_0\,\phi_1 = 0, \tag{24b}$$

where

$$\mathrm{L}_4 = \frac{\partial^2\boldsymbol{\Psi}_{\mathrm{B}}}{\partial x\,\partial y}(\mathrm{D}^2 + a^2)\,a - \frac{\partial^4\boldsymbol{\Psi}_{\mathrm{B}}}{\partial y^3\,\partial x}a.$$

Together with the homogeneous boundary conditions on ϕ_0 and ϕ_1 from (6*a*), equations (24) represent a coupled system of equations for the unknown quantities a_0, $\phi_0(y)$, a_1, $\phi_1(y)$. In contrast to previous formulations, this system simultaneously determines all quantities up to $O(R^{-1})$ in one step. Moreover, solving this system does not require the usual solvability condition and thus (24) provide a suitable zeroth-order approximation in a Landau expansion for finite amplitudes.

The solution of (24) can be obtained in different ways depending on the choice of normalization and numerical approach. We can directly impose the normaliation (8*b*) such that ϕ_0 and ϕ_1 are subject to the conditions

$$\frac{\mathrm{d}\phi_0(y_m)}{\mathrm{d}y} = 1, \quad \frac{\mathrm{d}\phi_1(y_m)}{\mathrm{d}y} = 0, \tag{25}$$

and solve the nonlinear system (24), e.g. by use of Newton's method.

An interesting alternative uses the approximation $a = \text{const}$, and hence $a_1 = 0$. Then (24a, b) form an eigenvalue problem for the single eigenvalue a_0 and eigenvector (ϕ_0, ϕ_1),

$$\begin{bmatrix} \mathrm{L}_0 + \mathrm{L}_1 & \mathrm{L}_2 \\ \mathrm{L}_4 & \mathrm{L}_0 \end{bmatrix} \begin{Bmatrix} \phi_0 \\ \phi_1 \end{Bmatrix} = \begin{Bmatrix} 0 \\ 0 \end{Bmatrix}. \tag{26}$$

As we will show in the discussion of the spectrum, the eigenvalue a_0 differs by $O(|a|R^{-1})^{\frac{1}{2}}$ from the corresponding eigenvalue of the Orr–Sommerfeld equation. Consequently, within the context of the local procedure, the approximation $a_1 = 0$ is effectively a normalization condition. This formulation of the local procedure allows one to determine easily the asymptotic form of the function $\phi(x, y)$ outside the boundary layer in the neighbourhood of x_0,

$$\phi(x, y \gg 1) = (x + \mathrm{i}Ky)\, \mathrm{e}^{\mathrm{i}ay}, \tag{27}$$

$$K = \frac{1}{1 - V_\infty/(\mathrm{i} + \omega/a)},$$

where V_∞ is the tranverse mean velocity far from the plate. This asymptotic behaviour is different from that of Orr–Sommerfeld solutions in parallel flows.

Finally, an iterative procedure can be utilized to solve the eigenvalue problem subject to conditions (25). This procedure starts with solving the Orr–Sommerfeld problem $\mathrm{L}_0 \phi_0 = 0$ to obtain an approximation to a_0 and ϕ_0. The next step solves (24b) together with the norm (25) on ϕ_1 for a_1 and ϕ_1 by using a solvability condition or solving the augemented system. The third step serves to find a new approximation to a_0 and ϕ_0 using the inhomogeneous equation (24a) and a second solvability condition. Up to this point, the iterative procedure leads to equations identical with those derived with the method of multiple scales (e.g. Saric & Nayfeh 1977). While the iterative procedure can be continued until the results converge to the solution of the simultaneous equations, it is consistent with the order of approximation to truncate after the third step.

For disturbances of long wavelength, the local procedure is inconsistent by keeping or discarding terms of equal order. This inconsistency arises when both a_0 is $O(R^{-1})$ and a_1 is $O(R^{-2})$. Then (24b), which can be seen as a 'closure' equation for the local procedure, is composed exclusively of terms of $O(R^{-2})$, which is inconsistent with (5) where terms of this order are neglected. The 'breakdown' of the local procedure in the limit of long wavelengths simply reflects the fact that it is not possible to obtain a solution to a partial differential equation of parabolic type using a Taylor-series expansion at a chosen streamwise location since the initial conditions cannot be accounted for. Long wavelengths occur at low frequencies and low Reynolds numbers, hence our observations agree with those of Itoh (1986) on the existence of a value of R, dependent on F, below which the disturbance equation (3) cannot be reduced to a set of ordinary differential equations.

The weaker dependence on the upstream conditions at the shorter wavelengths appears to be caused by a change in the character of the governing equations related to the dominance of the convective acceleration forces over viscous forces. At long wavelengths the convective and viscous terms are of equal order at every point across the boundary layer, as is the case in Prandtl's boundary-layer equations. At shorter wavelengths, however, the balance is limited to the wall and the critical layer – a fact used in the singular perturbation solutions to the Orr–Sommerfeld equation (e.g. Tollmien 1929) – while outside these layers the convective terms must balance each other 'locally' at every point along the streamwise direction. Solutions started

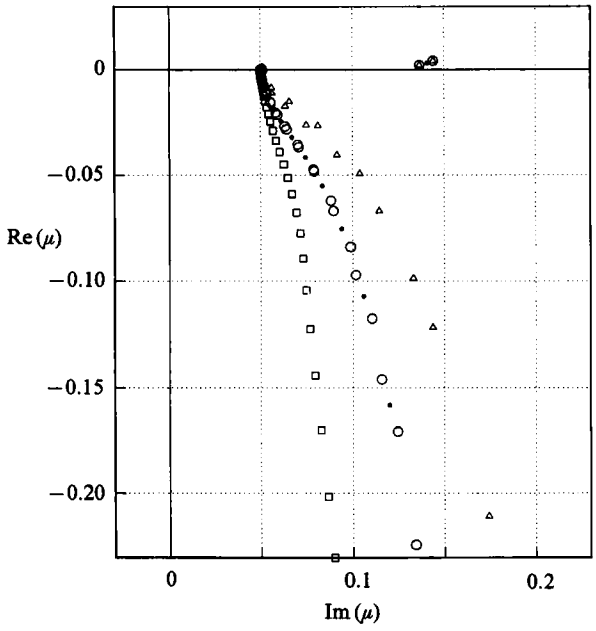

FIGURE 1. Spectrum of the spatial eigenvalues μ of (26) (△, $N = 25$; ○, $N = 40$) and of the Orr–Sommerfeld equation (●, $N = 40$; □, $N = 80$) for the Blasius boundary layer. $R = 500$, $F = 100$.

from different initial conditions asymptote downstream to a single solution, as shown in §4.2.

Initial conditions for transient-free marching solutions can be obtained at finite TS amplitudes by solving the nonlinear local problem. Using a Landau expansion procedure, the profiles ϕ_n, $\partial\phi_n/\partial x$ and exponents a_n in (9) are expanded in powers of A, where A is the amplitude of the fundamental wave ϕ_1, yielding a series of ordinary differential equations which can be solved in succession. The use of a well-defined amplitude A overcomes the non-uniqueness in determining the higher-order terms and avoids the restriction to almost neutral disturbances (Herbert 1980). The absence of a solvability condition in the treatment of the mean-flow non-parallelism allows this Landau expansion to solve concurrently for the effects of non-parallelism and finite amplitude (Bertoltti 1991).

Alternatively, one can prescribe initial conditions obtained by simpler means and accept the initial transients in the marching solution. If the initial amplitude of the TS wave is small, only the fundamental TS wave obtained from (24) needs to be given as initial condition; the harmonics are generated by nonlinearity during the marching process.

2.6. *The eigenvalue spectrum*

Typically, we use the least-stable eigensolution from the spectrum of the local procedure as initial conditions for the PSE. We discuss below the ways in which this spectrum differs from that of the Orr–Sommerfeld equation. The eigenvalue a appears up to fourth power in the matrix of the local procedure. The spectrum is accessible through standard software packages, such as EISPACK, provided the equations are reformulated into a larger system that contains the eigenvalue linearly (Gohberg, Lancaster & Rodman 1982, Bridges & Morris 1987). Figure 1 shows the spectrum for $R = 500$ and $F = 100$ together with the spectrum of the Orr–Sommerfeld equation (OSE). The local formulation splits each OSE eigenvalue into

a neighbouring pair of eigenvalues. The split is due to the perturbing effect of the operators L_1 and L_4 which are $O(R^{-1})$ and $O(|a|R^{-1})$, respectively. For further study of this phenomenon we fix all parameters, including the Reynolds number, and introduce $\epsilon = R^{-1}$ as a measure of the order of the terms in the operators L_1 and L_2, which are rescaled to $\hat{L}_1 = RL_1$ of order 1, and $\hat{L}_4 = RL_4$ of order $|a|$. The matrix (26) takes the form

$$\begin{bmatrix} L_0 + \epsilon \hat{L}_1 & L_2 \\ \epsilon \hat{L}_4 & L_0 \end{bmatrix} \begin{Bmatrix} \phi_0 \\ \phi_1 \end{Bmatrix} = \begin{Bmatrix} 0 \\ 0 \end{Bmatrix}. \tag{28}$$

Let $(\mu_1, \mu_2, \ldots)$ be the eigenvalues of L_0 with associated eigenvectors $(\phi_1, \phi_2, \ldots)$. Set ϵ to zero and call the resulting matrix $\boldsymbol{M}$. Since $\det(\boldsymbol{M}) = \det(L_0)\det(L_0)$, $\boldsymbol{M}$ has the eigenvalues of L_0 with multiplicity two and a single associated eigenvector of the form $(\phi_j, 0)^{\mathrm{T}}$. The splitting of μ_j into μ_{j1} and μ_{j2} can be expressed in a Puiseux series representation (Lancaster 1969),

$$\mu_{j1}(\epsilon) = \mu_j + c_{j1}\epsilon^{1/l} + d_{j1}\epsilon^{2/l} + O(|\epsilon|^{3/l}), \tag{29a}$$

$$\mu_{j2}(\epsilon) = \mu_j + c_{j2}\epsilon^{1/l} + d_{j2}\epsilon^{2/l} + O(|\epsilon|^{3/l}), \tag{29b}$$

where the subscripts j_1 and $j2$ refer to the two perturbed eigenvalues, and l is an integer less than or equal to the multiplicity of μ_j. In our case $l = 1$ or $l = 2$. The value of l was determined numerically by choosing the eigenvalue μ_j associated with unstable TS wave and tracing μ_{j1} and μ_{j2} as ϵ was varied from zero to R^{-1} in (28), holding R, and all other parameters, fixed. The results indicate that $l = 2$, and that the coefficients c_{j1} and c_{j2} are unequal and complex. The difference between the real parts of $\mu_{j1,j2}$ and μ_j is approximately the distance between the dashed and solid lines shown in figure 2. While the separation is of $O(R^{-1})$ for $R < 600$, at higher R it increases to $O(|a|R^{-1})^{\frac{1}{2}}$, as indicated by our analysis. In the next section we discuss the relevance of using one or the other of these two eigensolution for the initial conditions.

2.7. *Properties of the local and marching procedures*

The 'neighbouring pair' characteristic of the eigenvalues of the matrix (26) does not carry over to the physical growth rates. Figure 2 shows as dotted lines the variation with Reynolds number of the real part of the eigenvalues μ_a and μ_b corresponding to an amplified TS wave, and as solid lines the physical growth rate based on $u'_{\max}$ computed from these eigenvalues and their associated eigenvectors by (14a). While the real parts of the eigenvalues differ noticeably, the maximum difference in the physical growth rates is of the order of 10^{-4}, hence negligible. Both eigensolutions were used as initial conditions for the marching procedure. The marching results for both cases were found to be in agreement with each other and with the results of the local procedure. The filled and open circles in figure 2 denote the growth rate based on $u'_{\max}$ given by the marching procedure with the two sets of initial conditions.

The marching procedure is computationally more efficient than the local procedure by an order of magnitude. We have performed our calculations on a Cray-XMP/24. The marching procedure with 40 Chebyshev polynomials requires 0.06 s per step regardless of the step size. In contrast, the local procedure, using Newton iteration, converges in 0.38 s following a change in the Reynolds number and can only proceed in small steps.

An important consideration for the marching code is the variation of the accuracy with the streamwise step size. We tested the accuracy by comparing the result for $|\bar{a}(x)| = \bar{\gamma}^2 + \bar{\alpha}^2)^{\frac{1}{2}}$ based on $u'_{\max}$ at $R = 916$ after marhing from $R_0 = 400$ with different steps sizes. The most accurate value was assumed to be given by the smallest step size $\Delta x = 6$ and was used as a reference, $\bar{a}_{\mathrm{ref}}$. Step sizes ranged from $\Delta x = 6$ (256 steps)

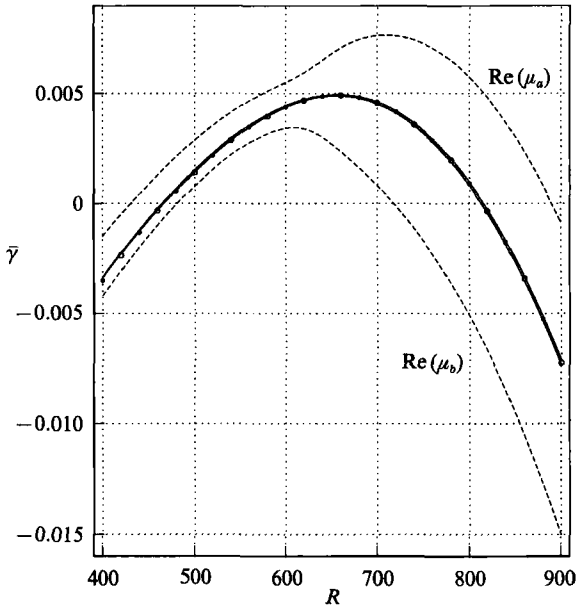

FIGURE 2. Variation of Re (μ_a) and Re (μ_b) with R of the pair of eigenvalues of the matrix (26) (dashed lines) and the growth rate $\bar{\gamma}$, (14*a*), of the associated eigensolutions (solid lines). ●, PSE, $u'_{\max}$ μ_a; ○, PSE, $u'_{\max}$ μ_b.

to $\Delta x = 486$ (4 steps). The difference $|\bar{a} - \bar{a}_{\text{ref}}|$ remains at $O(10^{-5})$ up to a step size of $\Delta x = 100$ (16 steps), and increases afterwards as $10^{-5}\exp(0.0125\,\Delta x)$ until reaching $O(10^{-3})$ at a step size of 377.7 (5 steps). At larger step sizes, the solution rapidly deteriorates.

3. The direct Navier–Stokes solution

The numerical method used here evolved from that presented by Spalart, Moser & Roger (1991), which has been applied to a variety of transitional and turbulent boundary layers. The algorithm, spectral in space and second-order accurate in time, was designed to solve the incompressible Navier–Stokes equations over a flat plate at $y = 0$ with periodic conditions in the directions x and z parallel to the plate. Because of the periodicity, the studies of spatially evolving flows could not be exact, and had to involve assumptions of slow growth of the boundary-layer thickness and disturbance energy, similar to those presented in §2 of this paper but more rudimentary (see the use of the group velocity by Spalart & Yang 1987). The streamwise evolution of the laminar flow as accounted for to a reasonable approximation, but the non-parallel effects (non-zero v-component) were not.

The new ingredient referred to as the fringe method, first applied to the Hiemenz flow (Spalart 1986), which allows the treatment of some truly spatially evolving, non-parallel flows with the same algorithm.

Let x be the direction in which the flow is not uniform, but for which the numerical method requires periodicity. The periodic domain $[0, \Lambda]$ is divided into a 'useful region' $[L, \Lambda - L]$ and two 'fringe regions' $[0, L]$ and $[\Lambda - L, \Lambda]$ at either end of the interval (by periodicity, these two regions can be regarded as one). The useful region is intended to cover the whole spatial history of a wave whereas earlier work with this code ontained only one or a few wavelengths. Let $U_{\text{B}}(x, y)$ be the laminar velocity

field; it satisfies the Navier–Stokes equations, in conjunction with a pressure field p_B. Split the velocity field $U(x, y, t)$ into a prescribed part $U_0(x, y)$ and a disturbance part $U_1(x, y, t)$,

$$U = U_0 + U_1. \tag{30}$$

The first step is to define a field U_0 that is periodic and smooth in x (at least two continuous derivatives) but coincides with the laminar flow in the useful region:

$$U_0(x, y) = U_B(x + x_0, y) \quad \text{for} \quad L < x < \Lambda - L. \tag{31}$$

Here x_0 is a parameter which allows us to locate the useful region in different parts of the laminar flow. For Blasius flow, the domain must start some distance downstream of the leading edge. A simple way to construct U_0 is to define a function $\hat{x}(x)$ which equals x on $[L, \Lambda - L]$ but is periodic with period Λ, and to write $U_0 = (u_0, v_0)$ with $u_0(x, y) = u_B(\hat{x} + x_0, y)$, $v_0(x, y) = (\mathrm{d}\hat{x}/\mathrm{d}x)\, v_B(\hat{x} + x_0, y)$. Naturally in the fringe U_0 is not a Navier–Stokes solution because $\mathrm{d}\hat{x}/\mathrm{d}x \neq 1$. It is not even essential to make it divergence-free. The function $\hat{x}$ is derived from a Gaussian (Spalart 1988).

The equations governing U_1 are the following:

$$\nabla \cdot U_1 = 0 \tag{32a}$$

$$\frac{\partial U_1}{\partial t} + U_0 \cdot \nabla U_1 + U_1 \cdot \nabla U_0 + U_1 \cdot \nabla U_1 = -\nabla p_1 + \nu \nabla^2 U_1 - d(x)\, U_1 + F(x, y, t). \tag{32b}$$

In the useful region, U_0 is a Navier–Stokes solution (i.e. $U_0 \cdot \nabla U_0 = -\nabla p_0 + \nu \nabla^2 U_0$), and d and F are both zero. A simple manipulation of (32) then shows that $U = U_0 + U_1$ satisfies the Navier–Stokes equations within that region, which was the objective.

The key assumption is that the non-physical phenomena occurring in the fringe do not invalidate the solution in the useful region. In general, the incompressible Navier–Stokes equations include long-range pressure interactions; however, in a shallow domain this range is only of the order of the smaller dimension, here the boundary-layer thickness δ. This is why the assumption $\delta \ll \Lambda$ is essential here, as it probably is for any numerical inflow–outflow strategy, or a wind tunnel for that matter (defining Λ loosely as the streamwise extent of the flow).

The role of the $-d(x)\, U_1$ term in (32b) is to damp the disturbances while they are in the fringe: d is a positive scalar function that rises smoothly from 0 in the useful region to a finite value in the fringe, typically a Gaussian. Assuming that the laminar flow is in the positive x-direction, the disturbances (i.e. U_1) are convected by U_0 into the fringe and their amplitude is reduced by orders of magnitude by the $-dU_1$ term. As a result the fluid that enters the useful region from the fringe, at $x = L$, is essentially free of disturbances, which amounts to the 'inflow condition' $U = U_0 = U_B$. We assume that the useful region and the fringe communicate only by convection of disturbances, and that information cannot travel upstream more than a few δ. In other words, on the scale of L and Λ, the equations have a parabolic behaviour.

The last term in (32b) is a prescribed body force $F(x, y, t)$, periodic in time and confined to a short region in x, that is used to generate waves in the flow (the analogue of a vibrating ribbon). With the present set up, adding a body force within the domain is more convenient than explicitly adding the perturbation to the inflow condition. In either case, there is no shape for the perturbation that is more justified than others. However, some shapes do generate waves in a smoother manner, resulting in a shorter transient in x before the wave is 'well developed' in the

sense of exhibiting a smooth growth rate (there is no rigorous concept of a 'pure' TS wave since the solution is fully two-dimensional). A fair choice is of the form $F_x = \partial\psi/\partial y$, $F_y = -\partial\psi/\partial x$, with

$$\psi = \epsilon \exp\left(-\frac{(x-x_r)^2}{\sigma_x^2} - \frac{y^2}{\sigma_y^2}\right) y^2 \cos(\omega t - \alpha x). \tag{33}$$

Here, ϵ is the amplitude of the force; σ_x and $_y$ are lengthscales in x and y; x_r is the position of the 'ribbon'; ω is the frequency of the wave; α is a wavenumber. The primary parameters are ω and $x_r + x_0$, and ϵ becomes important for nonlinear waves. The other parameters are chosen empirically to obtain a smooth transient; α is an estimate of the wavenumber of the wave, σ_x is of the order of the wavelength, and σ_y of the order of δ.

The function in (33) was constructed from a Guassian factor to make it fall rapidly but smoothly to zero, a y^2 factor to impose the boundary conditions at the wall, and a time-periodic wave-like dependence on t and x. The couple (F_x, F_y) is divergence-free. The boundary and divergence conditions are not indispensable in a body force, but if the divergence-free projection of F does not satisfy the no-slip condition, thin shear layers will appear at the wall and may degrade the numerical accuracy.

In the algorithm that solves (32*b*) for $\boldsymbol{U}_1$ the terms not found in the Navier–Stokes equations (two cross-terms with $\boldsymbol{U}_0$ and the d and $\boldsymbol{F}$ terms) are treated like the nonlinear term $\boldsymbol{U}_1 \cdot \boldsymbol{\nabla} \boldsymbol{U}_1$, by an explicit Runge–Kutta scheme (Spalart *et al.* 1991). This limits the magnitude of d for numerical stability; a typical peak value for $d(x)$ is $0.5/\Delta t$ where Δt is the time step. In a typical situation, $\boldsymbol{U}_1$ is reduced by three orders of magnitude while passing through the fringe (for our purpose there is no need to reset $\boldsymbol{U}_1$ exactly to zero). This can be achieved with $L \approx \Lambda/9$; thus, less than 25% of the domain is wasted.

In practice the functions d, $\hat{x}-x$, and $\boldsymbol{F}$ are not exactly zero in the useful region, since Gaussians are used. However, the parameters such as σ_x are chosen small enough relative to Λ that the residual values are negligible. Note also that since $\boldsymbol{U}_B$ is given by the Blasius equations, it is not exactly a Navier–Stokes solution. A higher-order approximation would require further assumptions about the outer flow and not be unique, and its stability properties would presumably differ very little from those of the basic Blasius solution.

The system given by (32) was programmed and tested, and the parameters such as L/Λ or σ_y/δ chosen, mostly empirically. One basic requirement is that the homogeneous system ($\boldsymbol{F} = 0$) be stable, which is not granted because of the streamwise amplification of the wave, and depends primarily on the d term and the width of the fringe. When this is true, we can start at $t = 0$ with $\boldsymbol{U}_1 = 0$ and activate $\boldsymbol{F}$. After a sufficient time (a few times Λ/U_∞) a time-periodic solution is obtained for $\boldsymbol{U}_1$. With infinitesimal amplitudes ϵ the nonlinear term $\boldsymbol{U}_1 \cdot \boldsymbol{\nabla} \boldsymbol{U}_1$ is inactive and the system behaves linearly; in particular, the periodic solution is accurately harmonic with frequency ω. Resolution tests, tests in which x_0 was varied, and moderate alterations of the ribbon parameters in (33) were all satisfactory. Another test is to use for $\boldsymbol{U}_B$ a parallel flow with Blasius profile. In that case exponential growth in x is obtained, with a growth rate close to that given by the Orr–Sommerfeld equation. Furthermore the growth rate is maintained up to the edge of the fringe at $\Lambda - L$, demonstrating that there is very little upstream influence of the extra terms in the fringe. This test also allows us to estimate the extent of the transient needed to the right of x_r to obtain a well-developed wave. Even with well-chosen parameters in (33), this extent is about $5 \times 10^4 \nu/U_\infty$ in x; as a result, it is impossible to firmly define

the leftmost part of the neutral curve, which is around $x = 9 \times 10^4 \nu / U_\infty$. In addition, it is much more difficult to obtain smooth and reproducible growth rates for decaying waves than for growing waves (this was to be expected, considering the existence of continuous-spectrum modes with arbitrarily small decay rates in the Orr–Sommerfeld equation).

Amplitude ratios for the wave amplitude from branch I to branch II of the order of e^5 have been obtained with $F = 50$. Much larger ratios, such as e^{10}, will eventually cause problems because even small numerical errors in the large-amplitude region will degrade the accuracy in the low-amplitude region. This would be true with almost all numerical methods, whether the errors propagate due to the global character of a spectral method, or to an implicit time integration scheme, or to the Poisson solver for the pressure. This numerical difficulty is absent in all the 'temporal' calculations, or in the parabolic theory presented in this paper.

We may compare the fringe method with that of Fasel (1976), which adresses the same problems. Unlike in Fasel's method, which is more conventional, we cannot declare simple inflow and outflow conditions such as Dirichlet, Neumann, or combination of derivatives. We verify that at the inflow the disturbance $\boldsymbol{U}_1$ is of much smaller amplitude the the disturbance that is intentionally input by the 'ribbon' (33). Thus, the solution is close to satisfying the Dirchlet condition that $\boldsymbol{U} = \boldsymbol{U}_B$ at $x = L$. At the outflow, the method achieves the objective of letting the disturbance smoothly leave the domain better than most conventional conditions, such as combinations of derivatives. Fasel's outflow condition relies on single-wave linear theory to such an extent that it cannot tolerate finite disturbances, nor even wave packets (Konzelmann & Fasel 1991; Rist & Fasel 1991). We conclude that the outflow condition implied by the fringe method is a little more obscure than the traditional ones, but is applicable to a much wider range of disturbances.

In terms of numerical efficiency, the cost per grid point and time step is comparable between the two methods, both running on Cray computers (U. Konzelmann & U. Rist, personal communication, 1991). Now the spectral method is recognized as being much more accurate per grid point. Stability calculations usually require 25 to 40 points in the y-direction (Spalart *et al.* 1991), compared with 105 points for Konzelmann & Fasel (1991), as an example. The waste of about 25% of the grid points in the x-direction is vastly offset by the extra accuracy, not to mention convenient numerical features such as decoupling of modes in the linear terms. Finally, note that the application of an efficient spectral method in y is quite dependent on the use of Fourier series in x (Spalart *et al.* 1991), which in turn is made possible by the fringe method.

Three cases were chosen to compare the theory and the numerical results. One case is linear and at relatively low frequency ($F = 50$) to show the effect of non-parallelism only, see figure 3. The other cases show both non-parallel and nonlinear effects. The results for the nonlinear evolution at $F = 86$ are shown in figures 11 and 12.

4. Results

The results are presented in two main parts, both focusing on the Blasius boundary layer. First, the role of non-parallelism on stability is isolated using small TS wave amplitudes in the direct simulation, and by solving the linearized version of the PSE, (6). Second, the evolution of finite-amplitude, two-dimensional disturbances is investigated.

As described above, the choice of the reference length δ_0 for non-dimensionalization

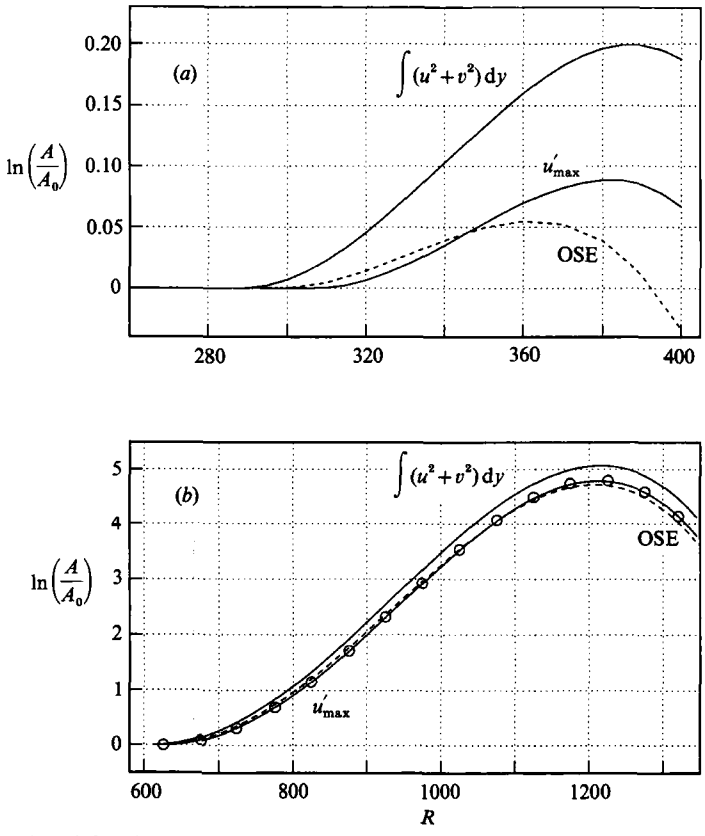

FIGURE 3. Amplification curves based on u'_{max} and the integral kinetic energy, (35), *vs.* Reynolds number R, at (*a*) $F = 220$ and (*b*) $F = 50$. Circles show results of the direct Navier–Stokes simulation.

is the value of $\delta(\tilde{x}_0)$ at the initial location of the marching calculations. Since this location varies from run to run, we remove this variation from the output data by non-dimensionalizing all results *a posteriori* with the local lengthscale $\delta(\tilde{x})$.

4.1. *Non-parallel effects*

Figure 3(*a*) and 3(*b*) show the amplitude variation of u'_{max} for TS waves at frequencies $F = 220$ and $F = 50$ calculated by the parallel theory (dashed), the non-parallel results for u'_{max}, (14*a*), and the integral of the kinetic energy, (35). The circles denote results for u'_{max} obtained by the direct Navier–Stokes simulation using a maximal TS amplitude of 10^{-8} to ensure linearity. The effects of non-parallelism are most visible at the higher frequencies, where the growth rates are small. At the lower frequency, all three curves are similar. In other words, non-parallel effects are insignificant at the lower frequencies where the TS waves undergo sufficient amplification to initialize secondary instabilities. The good agreement between the PSE and the DNS solutions reinforces our belief in the correctness of both methods.

We use the linearized parabolic stability equations (6) to duplicate the analysis of previous researchers, mentioned above. A similar, independent study can be found in Fasel & Konzelmann (1990), who analysed direct Navier–Stokes solutions of small-amplitude TS waves at four selected frequencies to arrive at conclusions in agreement with those presented here.

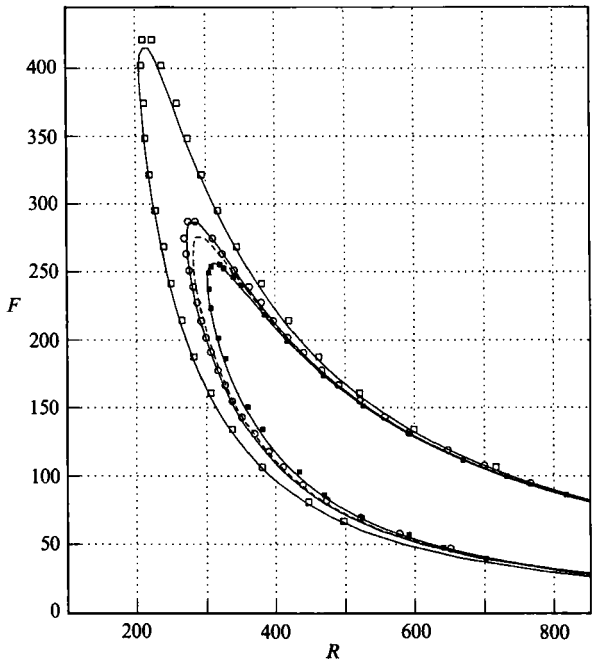

FIGURE 4. Neutral stability curves for Blasius boundary layer based on different measures of growth. Symbols mark the results of previous studies: □, Bouthier, equation (34); ○, Gaster, (35); ■, Gaster (14*a*). The solid and dashed lines denote results given by the PSE (36).

We begin the comparison with a listing of the definitions of growth that have been employed. Bouthier (1973) chose to measure growth in terms of the disturbance kinetic energy, $e_1 = u'^2 + v'^2$, and defined instability on a pointwise basis yielding a growth rate which varied with x and η. He computed growth rates from changes of e_1 along lines of constant η, consistent with his use of parabolic coordinates,

$$\gamma_B(x,\eta) = \frac{1}{2e_1}\frac{\partial e_1}{\partial x}\bigg|_\eta. \tag{34}$$

Bouthier presented two neutral curves. We consider the first curve that shows the points in the (RF)-plane for which instability was detected in at least one point across the boundary layer (usually at the wall); the second represents those points for which instability was detected in all points across the boundary layer.

Gaster's (1974) analysis seems the most penetrating and complete. His growth rate results are based on $u'_{\max}$, (14*a*), and on the integral of the disturbance kinetic energy

$$E(x) = \int_0^\infty [u'^2 + v'^2]\,\mathrm{d}y, \quad \gamma_G(x) = \frac{1}{E}\frac{\mathrm{d}E}{\mathrm{d}x}. \tag{35}$$

Saric & Nayfeh (1977) argued that both Bouthier's and Gaster's definition of the energy is incomplete by disregarding the product between the disturbance and the basic flow. We computed the neutral stability curve based on their definition of the energy (no results based on this quanity were given by Saric & Nayfeh):

$$e_2 = \left[\frac{1}{T}\int_0^T (2U_0 u + u^2 + v^2)^2\,\mathrm{d}t\right]^{\frac{1}{2}}, \quad \hat{E}(x) = \int_0^\infty e_2\,\mathrm{d}y, \quad \gamma_S(x) = \frac{1}{\hat{E}}\frac{\mathrm{d}\hat{E}}{\mathrm{d}x}, \tag{36}$$

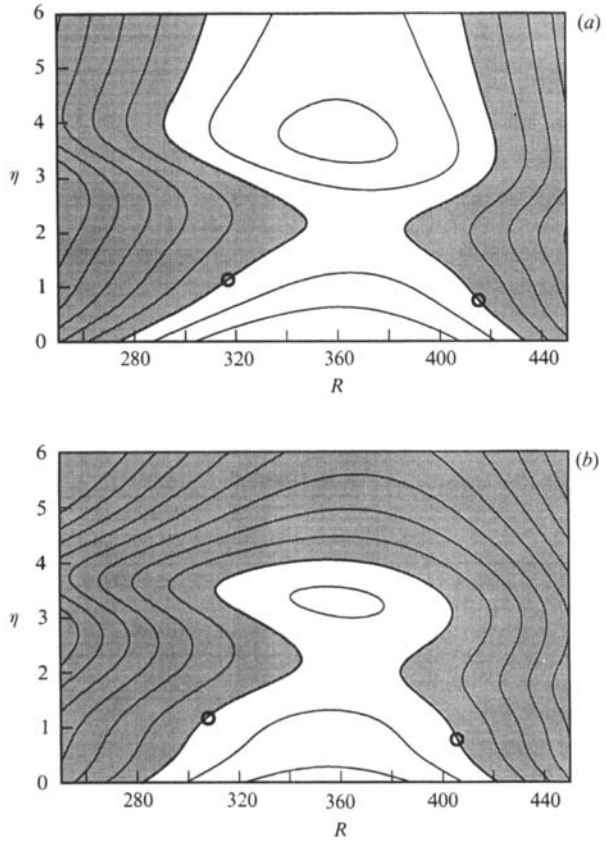

FIGURE 5. Iso-amplification lines based on the energy $u'^2+v'^2$, (34), at $F = 200$. Growth measured along lines of constant η. (*a*) PSE, (*b*) Orr–Sommerfeld equation. Circles denote position of $u'_{\max}$ at branches I and II.

where T is one period of the TS wave and time integration is used to obtain an r.m.s. value. Obtaining an r.m.s. value in time is simpler than in space, as chosen by Saric & Nayfeh.

We have applied all the definitions (34), (35) and (36), to the solutions of the linearized PSE. The resulting neutral stability curves are compared with published data in figure 4. The accurate duplication of published results points to both the correct formulation of their theories (i.e. ordering of terms) and to the accuracy of their solutions. The disagreement between published neutral curves must, then, be attributed to an incorrect comparison of different quantities, and we address this issue here.

Most of the effects Bouthier attributed to non-parallelism are really due to the direction of differentiation. To illustrate this point we have applied definition (34) to data furnished from the Orr–Sommerfeld equation. The results are shown in figure 5 in the form of lines in the (R, η)-plane on which the growth rate is constant, i.e. iso-amplification contours. The shaded regions are stable, while the regions in white are unstable. Both the contours from non-parallel calculations, figure 5(*a*), and the ones from the OSE, figure 5(*b*), show similar structure. In particular, both plots show maximum instability near or at the wall. For the parallel results one can show that at the wall, i.e. in the limit of $y \to 0$, definition (34) yields the growth rate $\alpha_{\mathrm{OSE}} - 1/(2R)$, showing clearly how (34) yields misleading values. The circles in figure

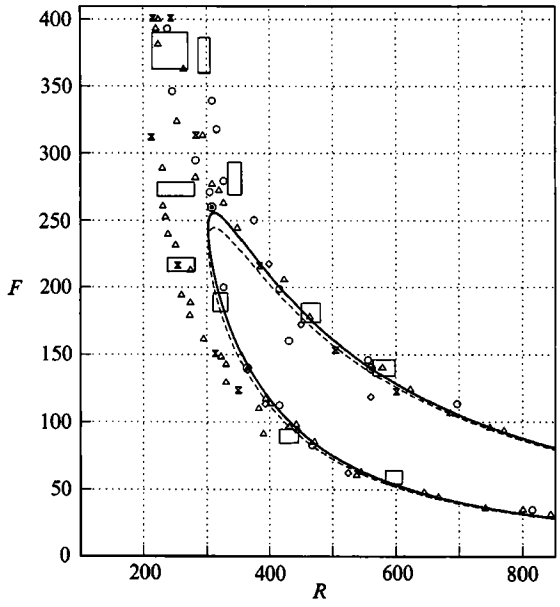

FIGURE 6. Comparison of experimental data and direct simulation data (based on u'_{max}) with the neutral stability curves for Blasius flow based on u'_{max} (solid line), u' at $\eta = 0.4$ (dashed line) given by PSE, and the Orr–Sommerfeld equation (dashed line). Experimental data: △, Ross *et al.* (1970); ○, Schubauer & Skramstad (1947); □, Strazisar *et al.* (1976); ⧖, Kachanov *et al.* (1977); ⊙, Fasel & Konzelmann (1990).

5(*a*, *b*) mark the position of u'_{max}. In figure 5(*b*), the circles also mark the branches I and II as given by the parallel theory, since at this point the direction of differentiation does not affect the growth rate.

Gaster's neutral curves based on u'_{max} and on (35) closely match the present results. The measurement of growth based on u'_{max} is of particular interest because most of the experimental data are based on the growth of u' at or near its maximum. Gaster compared his neutral curve based on u'_{max} with experimental data and concluded that the discrepancy at the high frequencies could not be explained. Our results are in agreement with his observation, as will be shown by figure 6.

The neutral stability curve based on (36) is shown in figure 4 as a dashed line. The difference in growth rates γ_G and γ_S is negligible, indicating that the effect of the term $2U_0 u$ in (36) is small.

Saric & Nayfeh (1977) presented a neutral curve based on the eigenvalue of the Orr–Sommerfeld equation plus its non-parallel correction as given by the method of multiple scales. Bridges & Morris (1987) have shown that the corresponding physical quantity is the normal component of velocity v measured at approximately $y = 2$, where the contribution by the profile $(1/v)(\partial v/\partial x)$ is zero. The usefulness for such a definition is limited, since the v-component of velocity is too small for direct measurements. Saric & Nayfeh also displayed growth rates based on u', differentiated along lines of constant η similar to those of Bouthier. These results are in agreement with ours, as shown in figure 7(*a*).

Figure 6 shows the neutral stability curves based on the growth of u'_{max} as defined by (14*a*), the growth of u' at $\eta = 0.4$ (along lines of constant η), and the neutral curve based on the Orr–Sommerfeld equation. Plotted as symbols are the experimental data of Ross *et al.* (1970), Schubauer & Skramstad (1947), Strazisar, Prahl &

Reshokko (1976) (the only data that show error bars), Kachanov *et al.* (1977), and Wortmann (1955), as reported in figure 1 of Saric & Nayfeh (1977). Also shown are the DNS results of Fasel & Konzelmann (1990), based on $u'_{\max}$. The computed curves differ from experimental data at lower Reynolds numbers and higher frequencies, and indicate that the discrepancy cannot be attributed to mean-flow non-parallelism. Indeed, comparison of the neutral curve based on $u'_{\max}$ with the curve given by the parallel calculations shows the effect of non-parallelism to be small for the two-dimensional disturbances considered here. The critical Reynolds number remains largely unchanged, and the overall effect of non-parallelism on the neutral stability curve is a slight extension to higher frequencies, and a small downstream shift of branches I and II. More importantly, the maximum growth rate in the non-parallel flow is close to the value given by the parallel theory, as shown in figure 3.

The source of the discrepancy between experimental and theoretical results for the neutral curve may be found in the details of the experimental measurements. Saric (1990) discusses numerous difficulties encountered in conducting accurate stability experiments. The difficulties intensify at frequencies above $F = 200$ due to the weak TS amplification. We contribute to this discussion by investigating the sensitivity of growth rates to four different effects:

(i) the distance from the wall at which the measurement is made;
(ii) the presence of a slight adverse pressure gradient;
(iii) the extent of transient response following altered initial conditions (as after the vibrating ribbon);
(iv) nonlinear effects at the amplitude levels used in the experiments.

Ross *et al.* (1970) measured the growth of the u'-component along lines of constant η at points below the maximum of u', thus altering the growth rate in the same way as Bouthier. Similarly, Schubacher & Skramstad measured growth along lines parallel to the plate at a location below the maximum of u'. Figure 7(*a*) shows the iso-amplification lines in the (R, η)-plane at a frequency $F = 200$ based on the u'-component of velocity and differentiation along lines of constant η. Figure 7(*b*) shows the lines obtained by differentiating along lines of constant y. The square in figure 7(*a*) denotes the location of the measurements of Ross *et al.* There, branch I is about $\Delta R = 20$ upstream of the value based on $u'_{\max}$ that is marked with a circle. This observation helps explain the systematic error $\Delta R = -20$ in the Reynolds numbers mentioned in their paper. The slope near the wall of the zero-amplification line indicates how measurements made near the wall lead to lower Reynolds number for branch I, and a higher one for branch II. The most unstable frequency is also increased, as seen in figure 6, where we display the neutral curve that results from measuring the growth of u' at the wall distance of $\eta = \tilde{y}/\delta(\tilde{x}) = 0.4$, along lines of constant η.

At y_m the growth rate is independent of the direction. Conversely, we investigated the growth rate along a family of lines of the form $y = x^c$ with $0 \leqslant c \leqslant \frac{1}{2}$, to see whether for any particular direction and streamwise position the growth rate is constant across the boundary layer. No such direction was found.

The sensitivity of the neutral curve for $u'_{\max}$ to an adverse pressure gradient is shown by the increase of the maximum unstable frequency from $F = 254$ in the Blasius boundary layer to $F = 346$ in a Falkner–Skan boundary layer with a pressure coefficient of $P = -0.02$, corresponding to the flow over a flat plate inclined by 1.8° to the free-stream direction. The change in the pressure coefficient is about 2% between branches I and II at the frequency $F = 50$. While an angle of 1.8° can be measured without difficulty, the effective inclination of the plate to the incoming

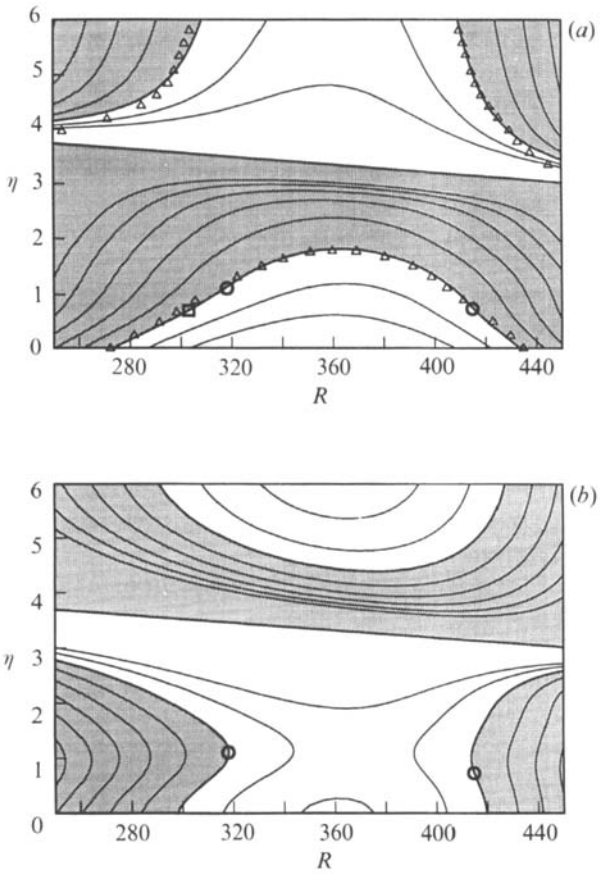

FIGURE 7. Iso-amplification lines based on the growth of u' for $F = 200$. Growth measured along (a) constant η, (b) constant y. Triangles indicate the results of Saric & Nayfeh (1977). Circles denote the position of u'_{max}, the square the position of the measurements of Ross *et al.* (1970). The flow is stable in the shaded areas.

stream is more difficult to detemine since the flow is affected by the growth of boundary layers along the wind-tunnel walls and can be obstructed by measuring devices in the test section.

Before advancing to the effects of transients and finite amplitudes, it should be noted that while the effect of non-parallelism of the evolution of two-dimensional waves is shown to be weak, the effect increases for three-dimensional waves as the direction of wave propagation veers away from that of the mean flow. At $F = 86$ the difference in total amplitude growth between the parallel and non-parallel calculations increase from 2.1% for a two-dimensional wave to 27% for waves inclined at 40° to the mean flow. At a propagation angle of 54° the non-parallel calculations show branch I and branch II separated by about 200 units in the Reynolds number, while the parallel-flow calculations do not display any region of instability. This results lead us to question if the experimental neutral points at high frequency were for three-dimensional rather than two-dimension waves. We found the destabilizing effect of non-parallelism on three-dimensional waves at the higher frequencies to be insufficiently strong to alter the result of Squire's theorem for parallel flows: the highest unstable frequency is reached by a two-dimensional wave. A full discussion on this subject can be found in Bertolotti (1991).

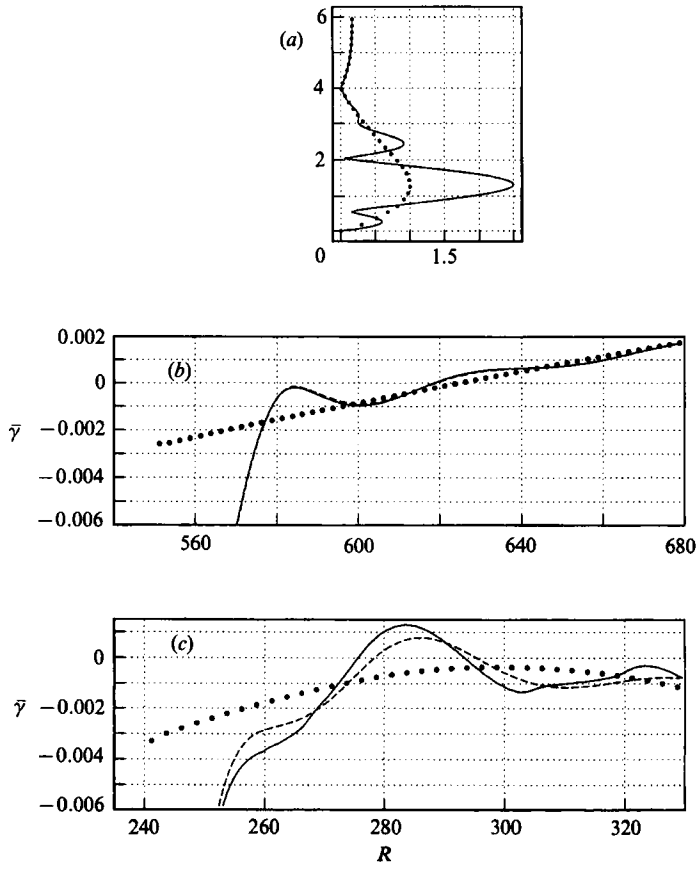

FIGURE 8. Transient solutions. (*a*) Distorted initial u' profile, (*b*) transient growth rate based on $u'_{\max}$ at $F = 50$, (*c*) transient growth rate at $F = 270$. Dots represent transient-free solutions. The solid and dashed lines in (*b*) and (*c*) indicate results for small and large step size, respectively.

4.2. *Transient analysis*

The generation of TS waves by a vibrating ribbon was investigated by Gaster (1965) and Aships & Reshotko (1990) who solved an initial-boundary-value problem associated with the Orr–Sommerfeld equation. The details of the events at, and near, the ribbon are beyond the scope of the present analysis which involves only one frequency. Instead, we address the speed of recovery of a disturbed TS wave profile to its undisturbed shape. This analysis is made possible by the ability of the PSE to account for the effects of upstream history on the solution.

The correct initial profile, ϕ_0, as given by the local procedure, was perturbed with a profile satisfying the boundary conditions but otherwise arbitrarily chosen in the form

$$\phi_{\mathrm{D}} = Ay^2 \mathrm{e}^{-y-\zeta y^2},$$

where the amplitude A is such that the maximum of the u'-component of the perturbation is 1.5 times the maximum of the undisturbed TS wave. The value of ζ is chosen to prevent any singularity at the initial location of marching (Hall 1983),

$$\zeta = \tfrac{1}{2} + a^{\frac{2}{6}} + \tfrac{1}{12}\mathrm{i}\omega \mathrm{R}.$$

As shown in figure 8(*a*), in comparison with the TS wave, the u'-component is perturbed mainly in the region below the point of phase reversal, the region most

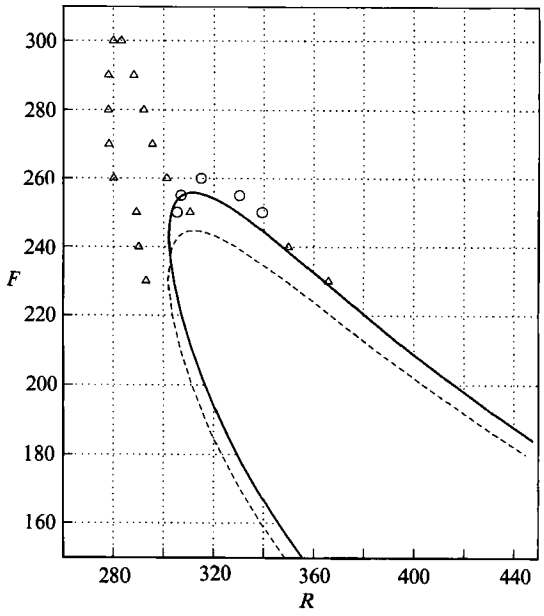

FIGURE 9. Alteration of neutral curve due to nonlinearity ($A = 1.4\%$) (circles) and transient behaviour (triangles). Solid and dashed lines indicate the neutral curves based on $u'_{\max}$ for PSE and OSE, respectively.

likely influenced by the vibrating ribbon that in experiments is typically located below the critical layer ($y \approx 1$). The initial value of the growth rate and wavenumber, a_0, was perturbed by increasing the theoretical value by 50%. The complete initial disturbance stream function was

$$\psi_0 = (\phi_0 + \phi_D) \exp(\tfrac{3}{2}\alpha_0 x - i\omega t).$$

The recovery to the unperturbed TS profile occurs within one wavelength λ_0. To be consistent with the parabolic approximation, very small step sizes were taken in the initial stages of marching. Two step sizes were used, $0.003\,125\lambda_0$ and $0.006\,25\lambda_0$. After marching over $\frac{1}{2}\lambda_0$, the step size was increased to $0.025\lambda_0$ and $0.05\lambda_0$, respectively.

Figure 8(*b*) shows the transient growth rate, based on $u'_{\max}$, at $F = 50$. The initial location x_0 is at $R = 550$, one wavelength upstream of branch I. The agreement between the solid and dashed lines corresponding to different step sizes shows that numerical effects are small. The transient growth rate shows branch I shifted upstream by a modest $\Delta R \approx -5$. The velocity profile at $x_0 + \frac{1}{2}\lambda_0$ closely resembles the undisturbed TS profile. This fast recovery indicates that, at least for our choice of perturbation, the evolution of the TS wave depends weakly on different initial conditions, unlike in the case of Görtler vortices, as discussed by Hall.

At higher frequencies, where amplification is weak, the growth rate oscillates about the unperturbed value for a longer downstream distance. Figure 8(*c*) shows the transient growth rates at $F = 270$. The oscillations are strong enough to display branches I and II at a frequency well above the neutral curve. The transient growth downstream of the ribbon could contribute to the distortion of the experimentally determined neutral curve at higher frequencies. The neutral stability curve given by our choice of perturbation function is shown in figure 9.

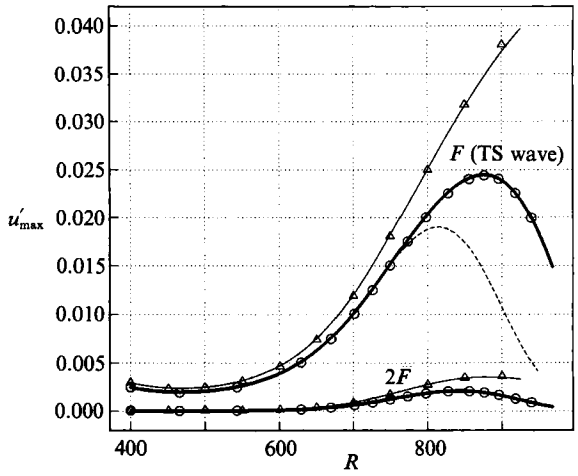

FIGURE 10. Amplitude of u'_{max} *vs.* Reynolds number R for TS waves at $F = 86$ and the first harmonic with $2F$ using initial TS amplitudes of 0.25% (heavy lines) and 0.30% (thin lines) at $R = 400$. The dashed line shows the linear result. Symbols denote results of the direct Navier–Stokes simulation.

4.3. *Nonlinear analysis*

One may also suspect nonlinear effects to contribute to the discrepancy between results and measured data. The experimental measurements of Ross *et al.* (1970) at higher frequencies have been performed at TS amplitudes u'_{max} of about 1.4%. A previous study (Herbert 1974) employing the parallel-flow approximation and temporal growth has shown that nonlinearity is destabilizing at the higher frequencies. Nonlinear non-parallel calculations based on a Landau expansion in the amplitude (Bertolotti 1991) confirm these results, but the shift with respect to the linear results is too small to account for the difference with experimental data. The circles in figure 9 show neutral stability points for a TS wave of 1.4% amplitude. We conclude that the discrepancy between experiment and theory for the neutral curve of the Blasius boundary layer can be attributed to neither non-parallel nor nonlinear effects.

The nonlinear evolution of a two-dimensional TS wave of frequency $F = 86$ was studied starting from $R = 400$ and marching downstream. Six Fourier components were used, with frequencies $0F$, $F, \ldots, 5F$. Two initial amplitudes where selected: $A_0 = 0.25\%$ and 0.30% (based on u'_{max} of the mode with frequency F). The results show that the effects of nonlinearity increase strongly with the amplitude. When $A_0 = 0.25\%$, the disturbance reaches a maximum amplitude of 2.44% at $R = 877$ and then decays. However, for $A_0 = 0.30\%$ the disturbance continues to grow past $R = 950$.

The variation of the u'_{max} amplitude with the Reynolds number is shown in figure 10. The upper heavy line is the amplitude of the TS wave for the 0.25% initial amplitude level, the lower heavy line is the amplitude of the $2F$ harmonic. The upper and lower thin lines show the corresponding quantities for an initial TS amplitude of 0.30%. The dashed curve shows the linear result for an initial amplitude of 0.25%. The circles and squares denote the values given by the full Navier–Stokes simulation and are in very good agreement with the PSE results. The velocity profiles at $R = 800$ for the case with 0.25% initial amplitude are shown in figure 11. For the

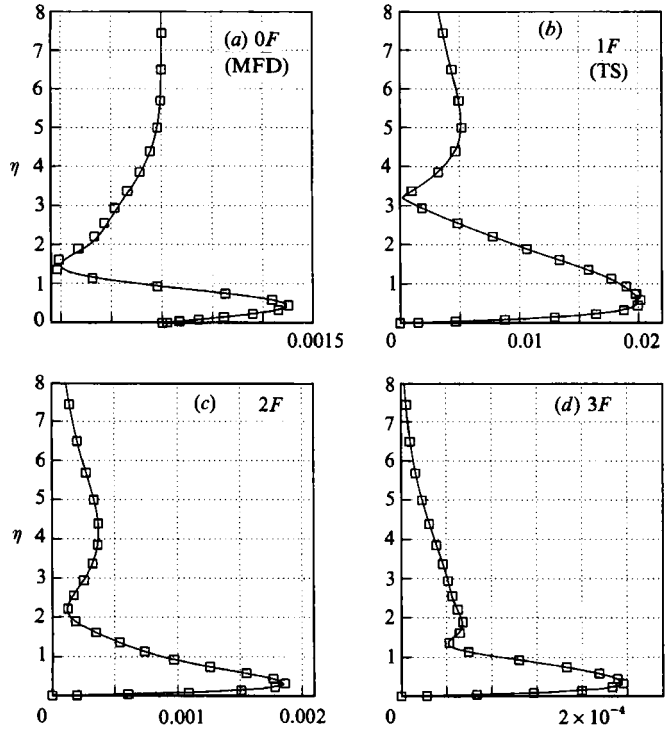

FIGURE 11. Velocity profile of (*a*) u (mean-flow distortion) and (*b–d*) u', at $R = 796$, $F = 86$, for an initial amplitude of 0.25% at $R = 400$. Symbols denote results of the direct Navier–Stokes simulation, lines the PSE results.

TS wave and the $2F$ and $3F$ harmonics the abscissa is the r.m.s. amplitude. The squares denote the values given by the full Navier–Stokes simulation. The good agreement between the nonlinear solutions to the PSE and direct Navier–Stokes solutions justifies the neglect of small terms in the PSE approach.

The destabilization of the TS wave by nonlinear effects in the neighbourhood of branch II and the continued growth as the amplitude exceeds some threshold value is consistent with the predictions of Itoh (1974) and Herbert (1974). Similar growth beyond branch II has been observed in Navier–Stokes solutions by Bayliss *et al.* (1985) and in the asymptotic analysis of Goldstein & Durbin (1986). The run with an initial amplitude of 0.3% is currently being continued with high resolution to clarify the fate of the flow in a strictly two-dimensional framework. In general, the two-dimensional flow is destroyed by strong secondary instabilities as the amplitude reaches levels of 1%.

The nonlinear effect on the growth rate is readily seen in figure 12 which shows the growth rate versus the amplitude $u'_{\max}$ at various Reynolds numbers ($F = 86$). The lines present the result of Landau expansions of orders A^5, A^7, and A^9, while the circles are given by the marching code, from various runs with different initial TS amplitudes. A small difference in growth rates given by the Landau and marching procedures persists as $A \to 0$ due inherent differences between local and marching results. Nonlinearity has a destabilizing effect for $R > 700$. The convergence of the Landau series is restricted to amplitudes of about 1% while the marching solution can be obtained for larger amplitudes, provided a sufficient number of harmonics is retained. The main shortcoming in the Landau procedure is the need for an ordinary

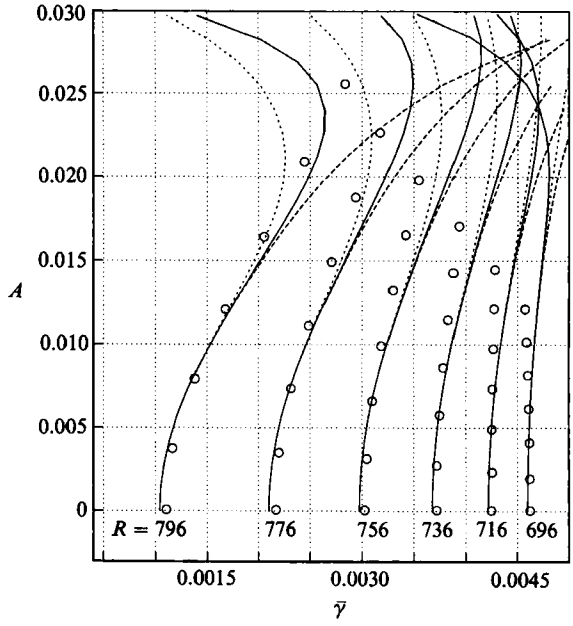

FIGURE 12. Variation of the growth rate $\bar{\gamma}$ with the amplitude u'_{max} at $F = 86$ and various Reynolds numbers. Lines denote results of the Landau expansion (----, A^5; – – – –, A^7; ——, A^9), circles results of the PSE obtained with different initial amplitudes.

differential equation that yields an acceptable approximation to the mean-flow distortion (see §2.5). We obtained an approximate equation by assuming that the profile is locally self-similar.

The marching code was primarily used on a Cray XMP/24. Although no special effort was made to optimize or vectorize the code and each Fourier component was approximated by 40 Chebyshev polynomials, the run times remained short: each of the two runs to generate the data shown in figure 10 required 162 s of CPU time, while the results of the linear analysis in figure 6 were obtained in less than 4 s.

5. Concluding remarks

Two new techniques for the analysis of boundary-layer stability are presented. One involves the direct solution of the Navier–Stokes equations, the other uses parabolic partial differential equations (PSE) for the stability analysis of convectively unstable flows. The latter approach offers numerous benefits over traditional methods based on normal modes and perturbation methods. The most noteworthy benefits are the ability to incorporate simultaneously mean-flow non-parallelism and nonlinearity and to correctly describe disturbances with long streamwise wavelengths. A local procedure is developed for the generation of initial conditions.

To clarify the diverse results of previous studies, we have used the PSE to investigate the effect of non-parallelism in the Blasius boundary layer. Our results show that this effect is small, in general agreement with the results of Gaster (1974) and Van Stijn & Van de Vooren (1983). The numerical results of Bouthier (1973) and Saric & Nayfeh (1977) can be reproduced, but the analysis shows that their definitions of growth rates are not based on relevant physical quantities, hence should not be compared with the existing experimental measurements.

The effect of finite amplitudes on growth rates has been considered. These nonlinear studies show that the maximum unstable frequency for finite-amplitude waves is higher than predicted by linear theory, but insufficient for explaining the experimentally observed amplification. The effect of initial transients on the evolution of TS waves is also considered. By arbitrarily distorting the initial conditions, we observe a region of transient growth which can alter the curve of neutral stability, suggesting a possible reason for the discrepancy at high frequencies between stability theory and experiments that use a vibrating ribbon to excite disturbances in the boundary layer.

An alternative approach for studying the spatial evolution of disturbances in boundary layers including nonlinear and non-parallel effects is the direct numerical solution to the Navier–Stokes equations. Special care must be taken to avoid using outflow boundary conditions which reflect a part of the energy of an outgoing disturbance. Herein we present a method for solving the full Navier–Stokes equation which uses buffer zones adjacent to the inflow and outflow boundaries and maintains the benefits of using Fourier series in the streamwise and spanwise direction.

The direct Navier–Stokes approach does not take advantage of the essentially parabolic character of the evolution of the disturbances, except in the fringe regions. This approach has an advantage and a disadvantage when compared to solving the PSE. The advantage is that the solution remains accurate all the way into turbulent flow, provided there is sufficient resolution, while the validity of the PSE may become questionable at the tertiary stages of transition after the appearance of spikes. The disadvantage is the enormous increase of memory and computational time needed. For this reason the PSE has practical applications. Results from the two approaches are compared as a first step in validation, and the agreement is found to be excellent.

Analysis based on the PSE has been extended to nonlinear, three-dimensional disturbances (Herbert 1991; Bertolotti 1991), and to compressible flow (Bertolotti & Herbert, 1991). The formulation in these works is a straightforward extensions of the one presented herein. Recently, the non-localized receptivity model of Crouch (1990) has been incorporated into the PSE (Crouch & Bertolotti 1992). We have limited our presentation herein to an incompressible flow in two dimensions, for clarity and emphasis of the basic concepts.

This work was supported by the Air Force Office of Scientific Research under Contract F49620-87-K-0005 (F.P.B. and T.H.) and by a NASA Training Grant NGT-50259 (FPB). One of the authors (P.R.S.) thanks Drs R. Moser and T. Poinsot of NASA Ames Research Center for valuable discussions.

REFERENCES

Ashpis, D. E. & Reshotko, E. 1990 The vibrating ribbon problem revised. *J. Fluid Mech.* **213**, 534–547.

Bayliss, A., Maestrello, L., Parikh, P. & Turkel, E. 1985 Wave phenomena in a high Reynolds number compressible boundary layer. *ICASE Rep.* 85–56.

Bertolotti, F. P. 1991 Linear and nonlinear stability of boundary layers with streamwise varying properties. Ph.D. thesis, The Ohio-State University, Columbus, Ohio.

Bertolotti, F. P. & Herbert, T. 1991 Analysis of the linear stability of compressible boundary layers using the PSE. *J. Theor. Comput. Fluid Dyn.* **3**, 117–124.

Bouthier, M. 1972 Stabilité linéaire des écoulements presque parallèles. *J. Méc.* **11**, 599–621.

BOUTHIER, M. 1973 Stabilité linéaire des écoulements presque parallèles : Part II. La couche limite de Blasius. *J. Méc.* **12**, 76–95.

BRIDGES, T. J. & MORRIS, P. J. 1986 Boundary layer stability calculations. *Phys. Fluids* **30**, 3351–3358.

CROUCH, J. D. 1990 A nonlinear mode-interaction model for boundary-layer receptivity. *Bull. Am. Phys. Soc.* **35**, 2262.

CROUCH, J. D. & BERTOLOTTI, F. P. 1992 Nonlocalized receptivity of boundary layers to three-dimensional disturbances. *AIAA Paper* 92-0740.

DRAZIN, A. P. & REID, A. W. 1981 *Hydrodynamic Stability*. Cambridge University Press.

FASEL, H. F. 1976 Investigation of the stability of boundary layers by a finite-difference model of the Navier–Stokes equation. *J. Fluid Mech.* **78**, 355–383.

FASEL, H. F. & KONZELMANN, U. 1990 Non-parallel stability of a flat-plate boundary layer using the complete Navier–Stokes equations. *J. Fluid Mech.* **221**, 311–347.

GASTER, M. 1962 A note on the relation between temporally-increasing and spatially-increasing disturbances in hydrodynamic stability. *J. Fluid Mech.* **14**, 222–224.

GASTER, M. 1965 On the generation of spatially growing waves in a boundary layer. *J. Fluid Mech.* **22**, 433–441.

GASTER, M. 1974 On the effects of boundary-layer growth on flow stability. *J. Fluid Mech.* **66**, 465–480.

GOHBERG, I., LANCASTER, P. & RODMAN, L. 1982 *Matrix Polynomials*. Academic.

GOLDSTEIN, M. E. 1983 The evolution of Tollmien–Schlichting waves near a leading edge. *J. Fluid Mech.* **127**, 59–81.

GOLDSTEIN, M. E. & DURBIN, P. A. 1986 Nonlinear critical layers eliminate the upper branch of spatially growing Tollmien–Schlichting waves. *Phys. Fluids* **29**, 2344–2345.

HALL, P. 1983 The linear development of Görtler vortices in growing boundary layers. *J. Fluid Mech.* **130**, 41–58.

HERBERT, TH. 1974 Über endliche Amplituden periodischer Störungen der Grenzschicht an der ebenden Platte. *DLR-FB* 74-53 (*ESA Tech. Transl.* TT-169, 1975).

HERBERT, TH. 1980 Nonlinear stability of parallel flows by high-order amplitude expansions. *AIAA J.* **18**, 243–248.

HERBERT, TH. 1991 Boundary-layer transition – analysis and prediction revised. *AIAA Paper* 91-0737.

HERBERT, TH. & BERTOLOTTI, F. P. 1992 Analysis of boundary-layer transition with parabolized stability equations. *J. Fluid Mech.* In preparation.

HERBERT, TH. & MORKOVIN, M. V. 1980 Dialogue on bridging some gaps in stability and transition research. In *Laminar–Turbulent Transition* (ed. R. Eppler & H. Fasel), pp. 47–72. Springer.

HUERRE, P. & MONKEWITZ, P. A. 1990 Local and global instabilities in spatially developing flows. *Ann. Rev. Fluid Mech.* **22**, 473–537.

ITOH, N. 1974 Spatial growth of finite wave disturbances in parallel and nearly parallel flows. Part 2. *Trans. Japan Soc. Aeron. Space Sci.* **17**, 175–186.

ITOH, N. 1986 The origin and subsequent development in space of Tollmien-Schlichting waves in a boundary layer. *Fluid Dyn. Res.* **1**, 119–130.

KACHANOV, YU. S., KOZLOV, V. V. & LEVCHENKO, V. YA. 1977 Nonlinear development of a wave in a boundary layer. *Fluid Dyn.* **3**, 383–390.

KONZELMANN, U. & FASEL, H. 1991 Numerical simulation of a three-dimensional wave packet in a growing flat plate boundary layer. In *Boundary Layer Transition and Control Conference, 8–12 April 1991, Cambridge. R. Aeronaut. Soc.*

LANCASTER, P. 1969 *Theory of Matrices*. Academic.

MCANINCH, G. L. 1986 Higher order parabolic approximations for sound propagation in stratified moving media. *AIAA J.* **24**, 253–260.

MORKOVIN, M. V. 1985 Guide to experiments on instability and laminar–turbulent transition in shear layers. *Course notes, AIAA Professional Study Series: Instabilities and Transition to Turbulence*. Cincinnati, Ohio.

Rist, U. & Fasel, H. 1991 Spatial three-dimensional numerical simulation of laminar-turbulent transition in a flat-plate boundary layer. In *Boundary Layer Transition and Control Conf. 8–12 April 1991, Cambridge, R. Aeronaut. Soc.*

Ross, J. A., Barnes, F. H., Burns, J. G. & Ross, M. A. S. 1970 The flat plate boundary layer. Part 3. Comparison of theory with experiment. *J. Fluid Mech.* **43**, 819–832.

Saric, W. S. 1990 Low-speed experiments: requirements for stability measurements. In *Instability and Transition*, Vol. 1 (ed. M. Y. Hussaini & R. G. Voigt). Springer.

Saric, W. S. & Nayfeh, A. H. 1977 Nonparallel stability of boundary layers with pressure gradients and suction. In *Laminar–Turbulent Transition, AGARD CP*-224, pp. 6/1–21.

Schubauer, G. B. & Skramstad, H. K. 1947 Laminar boundary-layer oscillations and transition on a flat plate. *J. Res. Natl Bur. Stand.* **38**, 251–292.

Smith, A. M. O. & Gamberoni, N. 1956 Transition, pressure gradient and stability theory. *Rep.* ES 26388. Douglas Aircraft Co., El Segundo, CA.

Smith, F. T. 1979*a* On the nonparallel flow stability of the Blasius boundary layer. *Proc. R. Soc. Lond.* A **366**, 91–109.

Smith, F. T. 1979*b* Nonlinear stability of boundary layers for disturbances of various sizes. *Proc. R. Soc. Lond.* A 368, 573–589 (and corrections: *Proc. R. Soc. Lond.* A **371**, 1980, 439).

Smith, F. T., Papageorgiou, D. & Elliot, J. W. 1984 An alternate approach to linear and nonlinear stability calculations at finite Reynolds numbers. *J. Fluid Mech.* **146**, 313–330.

Spalart, P. R. 1984 A spectral method for external viscous flows. In *Fluids and Plasmas: Geometry and Dynamics* (ed. J. E. Marsden). Contemporary Mathematics Series, Vol. 28. Am. Math. Soc., Providence RI.

Spalart, P. R. 1988 Direct numerical study of leading-edge contamination. In *Fluid Dyn. of 3D Turbulent Shear Flows and Transition, AGARD-CP*-438.

Spalart, P. R., Moser, R. D. & Rogers, M. M. 1991 Spectral methods for the Navier–Stokes equations with one infinite and two periodic directions *J. Comput. Phys.* (in press).

Spalart, P. R. & Yang, K. S. 1987 Numerical study of ribbon-induced transition in Blasius flow. *J. Fluid Mech.* **178**, 345–365.

Strazisar, A. J., Prahl, J. M. & Reshotko, E. 1975 Experimental study of the stability of heated laminar boundary layers in water *FTAS/TR*-75-113. Case Western Univ., Dept. Fluid Thermal Aerosp. Sci.

Tollmien, W. 1929 Über die Entstehung der Turbulenz. *Nachr. Ges. Wiss. Göttingen, Math-phys. Kl.*, pp. 21–44.

Van Dyke, A. M. 1975 *Perturbation Methods in Fluid Mechanics.* Parabolic.

Van Ingen, J. L. 1956 A suggested semi-empirical method for the calculation of the boundary layer transition region. *Rep.* UTHL-74. University of Technology, Dept. Aero. Engng.

Van Stijn, Th. L. & Van de Vorren, A. I. 1983 On the stability of almost parallel boundary layer flows. *Computers Fluids* **10**, 223–241.

Wortmann, F. X. 1955 Untersuchung instabiler Grenzschichtschwingen in einem Wasserkanal mit der Tellurmethode. In: *50 Jahre Grenzschichtforschung* (ed. H. Görtler & W. Tollmien). Vieweg.